Multiphysics Modelling of Liquid Crystal Based Adaptive Lenses

by

Alexandru Andrei Vasile

A thesis
presented to the University of Waterloo
in fulfillment of the
thesis requirement for the degree of
Master of Applied Science
in
Chemical Engineering

Waterloo, Ontario, Canada, 2020

Author's Declaration

This thesis consists of material all of which I authored or co-authored: see Statement of Contributions included in the thesis. This is a true copy of the thesis, including any required final revisions, as accepted by my examiners.

I understand that my thesis may be made electronically available to the public.

Statement of Contribution

This thesis contains work done using a existing numerical model to which I have made major contributions. The model was originally written by Fred Fu and expanded upon by Jake Ferguson, chapter 2 and chapter 4 of this thesis contains model equations whose derivations are attributable to Mr. Fu and Mr. Ferguson.

All other work in this thesis was performed by myself under the supervision of Professor Nasser Mohieddin Abukhdeir.

Abstract

Conventional lenses are limited by their fixed shaped and optical properties. Liquid crystal adaptive lenses (LCLAs) are a promising candidate to move beyond these limitations thanks their tuneable optical properties. A difficulty of working with LCs is that their properties are the result of an experimentally un-observable structure. Thankfully, modelling is capable of providing insight into this structure. Unfortunately, progress has been hamstrung by an over-reliance on experimentation. Further, what little modelling is being done usually involves simplified models and/or close-source software packages.

This work uses a general model for thermotropic nematic liquid crystals based on Landau-de Gennes theory to study the texture of liquid crystal adaptive lenses. The most general version of this model was used, without the common simplifications such as: hard anchoring, neglecting elastic constants, or geometric symmetry. In order to find the equilibrium state for the nematic model, the Euler-Lagrange equation for the total free-energy is set to zero. This form is converted into a transient PDE in order to capture the dynamics of the system, and to evolve the texture towards its equilibrium state. The nematic model is coupled with a model for the electric field within the cell, and the two are solved simultaneously. This is accomplished by using the method of lines for temporal discretization and the finite element method for spatial discretization.

The validity of the implemented model was first verified by modelling two important LCD configurations: the TN cell and the IPS cells. The TN cell was modelled with the electrodes off and with them on. In both cases the correct equilibrium texture was obtained. Modelling light propagation with cross-polarization microscopy produced the correct results, a bright cell when the electrodes were off and a dark one when they were on. Next, the IPS cell was also modelled. Again, the correct equilibrium result was obtained; a twisted texture was when the electrodes are turned off and an untwisted texture when the electrodes are turned on. Modelling light propagation resulted in the correct dark state when the electrodes were off andthe correct bright state when they were on.

Having successful produced the expected texture and cross-polarization microscopy results, the model was applied to a LCAL. The literature review of this work identified a wide range of potential liquid crystal adaptive lenses. The final design was chosen using three criteria: 1) availability of published results, 2) modelling requirements, and 3) ease of manufacture. Based on these criteria, a design called the HMD cell was chosen. When modelled, the resulting texture and cross-polarization microscopy did not agree with previously published results. An investigation into the cause of these discrepancy was performed, but the cause has not yet been identified.

Acknowledgements

Firstly, I would like to thank Professor Nasser Mohieddin Abukhdeir for his ongoing support throughout these two years.

I would also like to thank Frank Fu, whose initial work formed the basis of the model used in this thesis. Additionally, I would like to thank Jake Ferguson for excellent augmentations of Fu's work Next, I would like to specifically thank Thomas Donnelly, James Lowman, and Kimia Entezari for their feedback, expertise, and friendship. As well as the COMPHYS group as a whole for the great team environment and camaraderie.

I would like to acknowledge the following sources of funding that supported both me and this research over the past two years: the Natural Sciences and Engineering Research Council of Canada (NSERC) through their CGS M scholarship, the faculty of engineering through their Engineering Fellowship, the Waterloo Institute of Nanotechnology (WIN) through their WIN Nanofellowship, and the department of chemical engineering.

Lastly, I would like to thank Compute Canada, without whose compute sources I would not have been able to perform the modelling required for this work.

Dedication

To my family.

Table of Contents

List of Figures x

List of Tables xiii

1 Introduction 1

1.1 Research Motivation . . . 1

1.2 Objectives . . . 2

1.3 Thesis Structure . . . 3

2 Background 4

2.1 Electromagnetism . . . 4

2.1.1 Light waves and rays . . . 4

2.1.2 Refraction . . . 5

2.1.3 Polarization of Light . . . 6

2.1.4 Maxwell's Equations . . . 8

2.1.5 Electrostatics . . . 8

2.2 Liquid Crystals . . . 10

2.2.1 Properties . . . 10

2.2.2 Defects . . . 12

2.2.3 Experimentally Observable Properties . . . 13

2.2.4 Applications . . . 14

2.3 Lenses . . . 15
2.3.1 How Lenses Work . . . 15
2.3.2 Types of Conventional Lenses . . . 15
2.3.3 Types of Adaptive Lenses . . . 18
2.3.4 Lens Design History . . . 20
2.4 LC Modelling . . . 22
2.4.1 Order Parameters . . . 23
2.4.2 Frank-Oseen Theory . . . 27
2.4.3 Landau-de Gennes Theory . . . 29

3 Literature Review **33**
3.1 Design Considerations . . . 34
3.1.1 Modes of Control . . . 34
3.1.2 Lens Shapes . . . 36
3.1.3 Shape and Number of LC Domains . . . 38
3.1.4 Polarization Independence . . . 38
3.2 Consequences of LCAL Design Choices on Modelling . . . 39
3.3 LCAL Modelling Work in Literature . . . 40
3.4 Applications . . . 41

4 Methods **44**
4.1 Model Formulation . . . 44
4.1.1 Coupling of Electric Field and Molecular Orientation . . . 45
4.1.2 Free-Energy Minimization . . . 45
4.2 Numerical Methods . . . 46
4.2.1 Finite Element Implementation . . . 46
4.2.2 Time Stepping . . . 47
4.2.3 Periodic Domain . . . 48
4.2.4 Boundary and Initial Conditions . . . 48
4.3 Cross-Polarization Microscopy . . . 48

5 Modelling of LCD Cells **50**
5.1 Background . . . 50
5.1.1 TN Cell . . . 50
5.1.2 IPS Cell . . . 51
5.2 Methodology . . . 53
5.3 Results . . . 54
5.3.1 TN Cell . . . 54
5.3.2 IPS Cell . . . 55
5.4 Summary . . . 58

6 Modelling of a LCAL **60**
6.1 Background . . . 60
6.1.1 Criteria for Choosing a LCAL . . . 60
6.1.2 The HMD Cell . . . 61
6.1.3 Previous Modelling Work . . . 64
6.2 Methodology . . . 65
6.3 Results . . . 66
6.4 Investigation the Discrepancy in Results . . . 69
6.5 Summary . . . 70

7 Conclusions **72**
7.1 Conclusions . . . 72
7.2 Recommendations . . . 73

References **74**

APPENDICES **88**

List of Figures

2.1 Light ray propagating through space with the electric field shown. Left showing the x-z plane, right showing the x-y plane with the light ray coming out of the page. 5

2.2 Light refracting at an interface due to a change in medium. From [9]. . . . 5

2.3 Different polarization diagrams and phase difference changes. (a) $A_y = A_x$, (b) $A_y = 2A_x$. From [13]. 7

2.4 Different thermotropic LC mesophases. From [14]. 11

2.5 Uniaxial LC ellipsoid with parallel and perpendicular permittivity values labelled. After [8]. 12

2.6 Several types of defects. Lines are director streamlines. From [16]. 13

2.7 Cross-polarization microscopy with an optically active sample. 14

2.8 Two conventional lenses, (a) a converging lens, (b) a diverging lens. After [20, 21]. 16

2.9 Small lens employing multiple aspherical lens elements. From [22]. 17

2.10 A spherical lens (right) and the equivalent Fresnel lens (left). From [23]. . . 17

2.11 An adaptive lens in two configurations: (a) A converging lens, (b) A diverging lens. After [20, 21]. 19

2.12 A LCAL in multiple modes: (a) Turned off, (b) Converging Lens, (c) Beam Steering. From [25]. 19

2.13 Index of Refraction Distribution in a LCAL: (a) Lens off, (b) Diverging Lens, (c) Converging Lens. From [26]. 20

2.14 An example of a late 19th century lens, the Cooke triplet. From [27]. . . . 21

2.15 An example of a late 20th century lens made using computer aided design. From [28]. 22
2.16 (a) Molecular orientation, where $\hat{n}$ is the director and $\hat{u}$ is orientation of a particular molecule, (b) orientation distribution corresponding to low (dashed-black) and high (solid-red) degree of ordering. From [8]. 24
2.17 (a) Molecular axis point to position on unit sphere, (b) equal probability contours for uniaxial alignment (blue) and biaxial alignment (red). From [8]. 25
2.18 Visual representation of the Frank-Oseen constants. (a) k_{11}, k_{22}, and k_{33} from [14], (b) k_{24} from [16]. 28

3.1 A LCAL in three different configurations: (a) lens powered off, (b) converging light, (c) diverging light. After [58]. 35
3.2 Electrode configuration for a simple cylindrical LCAL. From [64]. 36
3.3 Electrode configuration: (a) hole-patterned electrode from [69], (b) spherical ring electrode from [70]. 37
3.4 Electrode configuration for a Fresnel LCALs: (a) top-down view from [75], (b) side view from [78]. 38
3.5 Designs of polarization independent LCALs with homeotropic anchoring: (a) curved surface, from [79], (b) negative permittivity anisotropy LC, from [84]. 39
3.6 Vergence-accommodation conflict visualized. From [119]. 43

5.1 Texture of a TN cell in the light state (left) and dark state (right). From [128]. 51
5.2 The interdigitating electrode structure. From [129]. 52
5.3 An IPS cell in its dark and light states, left and right respectively. From [130]. 52
5.4 Equilibrium texture model results of the TN cell with the: (a) electrodes off, (b) electrodes on and view parallel to bottom anchoring direction, (b) electrodes on and view parallel to top anchoring direction. 54
5.5 Cross-polarization result of TN cell, (a) Electrodes turned off, (b) Electrodes turned on. 55
5.6 Texture of IPS cell. Electrodes off: (a) side view, (b) bottom view of bottom surface. Electrodes on: (c) side view, (d) bottom view of bottom surface. . 56

5.7 Cross-polarization result of IPS cell, (a) Electrodes turned off, (b) Electrodes turned on. 58

6.1 Exploded diagram of the HMD cell, showing the LC layer and the orientation of the interdigitating electrodes. From [67]. 61

6.2 Top-down view of the HMD cell: (a) electrodes and cell parameters labelled, (b) view showing the overlap of the electrodes on either side of the LC layer. From [134]. 62

6.3 Side view layer with single cylindrical lens showing the texture and how it would expand light. From [67]. 63

6.4 Comparison of the equilibrium texture along the x-y plane at $z = 0.6d$: (a) this work, (b) from [135]. 66

6.5 Comparison of the equilibrium texture along the y-z plane in the centre of the square aperture. (a) this work, (b) from [135]. 67

6.6 Cross-polarization results. Top row: polarizer and analyzer running horizontally and vertically with respect to the page. Bottom row: polarizer and analyzer at -45° and 45° with respect to horizontal. 68

List of Tables

5.1 TN cell parameters 53
5.2 IPS cell parameters 53

6.1 Physical cell parameters 65

A.1 LC parameters for 5CB 88
A.2 LC parameters for E7 89
A.3 LC parameters used for the unspecified nematic 89

Chapter 1

Introduction

1.1 Research Motivation

The need and desire to manipulate light in ever more complicated, precise, and economical ways has spurred great progress in the fields of optics, material science, and computational modelling. As researchers strive for ever smaller and more powerful lenses, materials with better optical properties, such as a larger index of refraction, have been sought out. As the design of each lens element has become more advanced, so too has the entire lens system; where once it consisted of 3 lens elements [1], upwards of 10 elements is now commonplace [2, 3].

Commonly available mass-produced lenses are characterized by lens elements of a fixed focal length. In a multi-element lens systems, such as in cameras, focusing and zooming is achieved by physically moving some of the lens elements relative to the others. For systems with a single element, such as eyeglasses, focusing is achieved by the eyes themselves and zooming in/out is not possible. Additionally, if the a person's eyes are bad enough they will require multiple pairs of glasses (i.e. reading and distance glasses), bifocal, or progressive glasses.

Conversely, state of the art lens technology is adaptive. Adaptive lenses elements have focal lengths and optical properties which can be dynamically controlled. These lens elements allow for more compact designs and increased reliability since elements no longer move in order to focus and zoom. Additionally, fewer elements are needed in order to achieve the same optical results. Adaptive lenses, through their ability to change their focal length, allow for elegant solutions to engineering problems such as zooming without movement in a camera lens and eye glasses which dynamically adjust for viewing distance.

Several approaches exist for adaptive lenses using shape-changing designs, such as liquid between deformable- membranes [4] or electrowetting [5]. The drawback of such approaches is that they are not mechanically stable and, consequently, an applied force, such as due to acceleration, will cause them to deform and deviate from the desired optical properties. Additionally, the potential for leaks is ever present as they both use liquids.

Another approach for adaptive lenses involves fixed-shape lenses, which have high mechanical stability. Liquid crystal (LC) based adaptive lenses (LCAL) are part of this category. In addition to their mechanical stability, LC-based adaptive lenses leverage the mature liquid crystal display (LCD) market; a technology with decades of industrial expertise and which is already commercialized and mass-produced.

One of the main challenges of doing research with LCs is that the resulting molecular orientation is extremely difficult to observe *directly*. There exist some techniques for doing so [6], but their complexity and time requirement make them unfeasible for large scale engineering design. The alternative has been to observe the optical response of the LC and then infer the "texture", the overall orientation of the molecules, that would create this response.

This motivates the use of theory and modelling. These approaches provide *direct*, while approximate, observations of the LC texture. However, the models are challenging to solve numerically due to their highly non-linear and multiphysics nature as well as the significant variation in length scales. Specifically, domain length scales are on the order of millimetres to centimetres but require a resolution on the order of nanometres in order to capture potential topological defects.

1.2 Objectives

In order to enable engineering design of LC lenses informed by a direct understanding of molecular orientation, a computationally tractable mathematical model that captures all of the relevant physical phenomena, optical response, and lens characteristics is needed. To that end, the overall aim of this work is to study the texture and resulting optical response of liquid crystal adaptive lenses through the use of modelling. Specific objectives include:

1. Improving an existing multiphysics transient tensorial Landau-de Gennes model, initially implemented by Fu [7] and expanded on by Ferguson [8], in order to apply it to liquid crystal lens geometries.

2. Incorporate cross-polarization microscopy modelling so the results can be directly compared to experimentally observable results.

3. Validating the model by recreating known LCD configurations: the TN and IPS cell.

4. Validating the model by recreating published results of a LC lens.

1.3 Thesis Structure

This thesis is organized into 7 chapters. The first chapter outlines the research motivations and objectives for the thesis. Chapter 2 provides theoretical background on electromagnetic waves, optics, liquid crystals, liquid crystal applications, and theoretical models for liquid crystals. Chapter 3 is a literature review of the history and types of liquid crystal lenses, past modelling of liquid crystal lenses, and applications of liquid crystal lenses. Chapter 4 describes the mathematical and numerical methods used to solve the theoretical equations laid out in Chapter 2, and describes the visualization methods that will be used. Chapter 5 will validate the model and visualization technique using standard LCD geometries, the TN and IPS cell. Chapter 6 will introduce a liquid crystal lens to model, discuss past work on this design—and it's shortcomings, and then model it and discuss the results. Chapter 7 summarizes the conclusions and recommendations for future work.

Chapter 2

Background

This chapter will summarize the necessary background knowledge needed to understand lensing, the basics of nematic liquid crystals, and the theoretical models for nematic liquid crystals. First, a brief background on electromagnetism, as it relates to lenses and liquid crystals, will be presented. Then, liquid crystals and their properties will be discussed. Following this, the principles of lensing, different ways of producing lenses, and the need for computer modelling in lens design will be summarized. Finally, the modelling of nematic liquid crystals using a vector and tensor representation will be presented.

2.1 Electromagnetism

2.1.1 Light waves and rays

Electromagnetic waves, including visible light, are composed of two transverse waves, the electric and the magnetic. For simplicity, in general application light is often discussed as a being a ray, rather than a wave. This ray consists of a direction of propagation, and an associated index of refraction, more of than in the next subsection. Figure 2.1 shows the electric wave and its corresponding ray representation; note that the magnetic wave was omitted. This simplification is not compatible with LC optical research due to the anisotropic nature of LCs as will be shown over the following subsections.

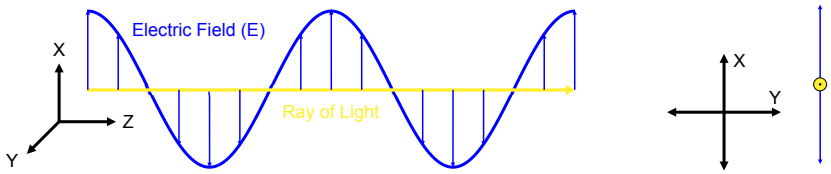

Figure 2.1: Light ray propagating through space with the electric field shown. Left showing the x-z plane, right showing the x-y plane with the light ray coming out of the page.

2.1.2 Refraction

Refraction refers to the change in a wave's direction caused by a change in its speed. For light rays, this occurs due to change in the index of refraction; either due to a change in medium, or change in the index within a medium. Figure 2.2 below shows a light way refracting due to a change in medium.

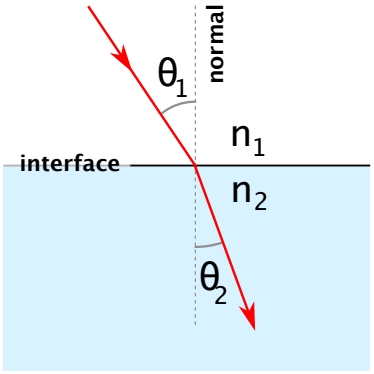

Figure 2.2: Light refracting at an interface due to a change in medium. From [9].

This behaviour is quantified by Snell's law [10]:

$$\frac{\sin(\theta_2)}{\sin(\theta_1)} = \frac{n_1}{n_2} \tag{2.1}$$

where θ_i is the angle measured between the ray of light and the surface normal in medium i, and n_i is the refractive index of medium i. The index of fraction, n, of a medium is defined as the ratio of the speed of light in a vacuum, c, to that in the medium, v:

$$n = \frac{c}{v} \tag{2.2}$$

An index of a refraction is associated with ray representation of light, but it is related back to and calculated from material properties associated with the wave representation of light as follows:

$$n = \sqrt{\varepsilon_r \mu_r} \tag{2.3}$$

where ε_r is the relative permittivity of the medium, the ratio of its permittivity to the permittivity of vacuum (related to the electric field), and μ_r is the relative permeability of the medium, the ratio of its permeability to the permeability of vacuum (related to the magnetic field). Both ε_r and μ_r are frequency dependant, but in the visible spectrum $\mu_r \approx 1$ for common non-magnetic material, and is therefore often omitted when converting between n and ε_r.

Isotropic material have a single value for their relative permittivity regardless of the direction in which the electric wave oscillates through the material. Anisotropic materials on the other hand have a relative permittivity which is dependant on the direction of oscillation, the wave's polarization.

2.1.3 Polarization of Light

The functionality of a conventional lens is not influenced by the direction in which the electric wave oscillates, but the functionality of a LCAL is. Distinguishing between them is therefore very important. As mentioned previously, the electric field oscillates perpendicular to the direction of propagation, e.g. in Figure 2.1 it oscillates along the x-y plane. However there are an infinite number of waves which oscillate along the x-y plane that can be represented by the same light ray propagating in the z-direction.

The oscillation of the electric field, and specifically its shape, is referred to as the polarization of the field [11, 12]. The wave in Figure 2.1 oscillates only along the x-direction, so it is referred to as linearly polarized light. When a beam of light is made up of individual waves which all have the same polarization, the beam as a whole is polarized. Conversely, when the beam of light is made up of individual waves which each have different polarizations, the beam is referred to as unpolarized; the electric field will appear to oscillate randomly.

When the oscillation is not random, the wave will appear to trace one of three shapes: a line, a circle, or an ellipse. In addition to shape, there are two further characteristics: rotation direction and angle of tilt. The rotation direction applies to circularly and elliptically polarized light. It describes the direction in which the shape is drawn, either

clockwise or counter-clockwise. The angle of tilt applies to elliptically and linearly polarized light. It refers to the angle made between the long axis of the ellipse (or the line) and the horizontal/vertical axis.

To mathematically describe polarization, we must first describe the electric field. For a polarized wave propagating in the z-direction, at a point in space, as a function of time, the two components of the electric field are:

$$E_x(t) = A_x \sin(\omega t) \tag{2.4}$$
$$E_y(t) = A_y \sin(\omega t + \delta) \tag{2.5}$$

where A_x and A_y are the amplitudes of the x and y components, respectively, ω is the angular frequency, and δ is the phase shift between the x and y components of the field.

Figure 2.3 shows the polarization states for corresponding to different values of δ, A_x, and A_y. From it, we can see that δ controls both the shape of polarization and rotation direction, while the ratio of the amplitudes, A_x/A_y, controls the tilt.

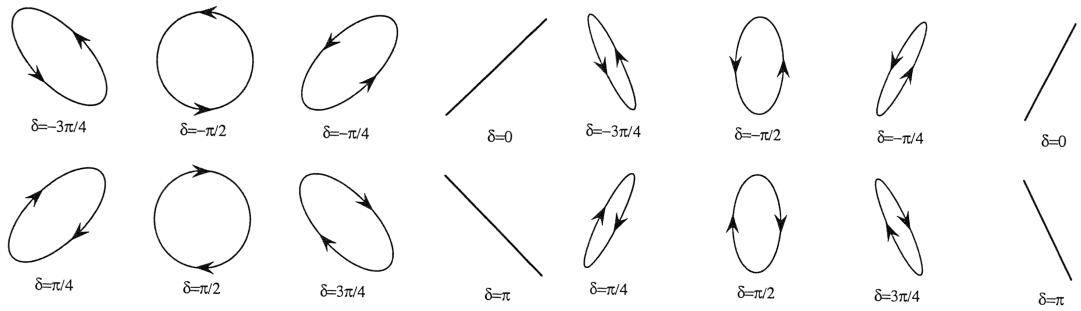

Figure 2.3: Different polarization diagrams and phase difference changes. (a) $A_y = A_x$, (b) $A_y = 2A_x$. From [13].

Not only does the polarization of an EM wave impact its interaction in with anisotropic medium, but an anisotropic medium can impact the polarization of the wave. The first way in which this can occur is with an anisotropic material with spatially constant indices of refraction. If polarized light with $\delta = 0$ enters such a medium one component is slowed down more than the other, thus the two components will complete a different number of cycles before exiting the medium and thus exit out of phase, i.e. $\delta \neq 0$. The second way is in an anisotropic medium with a spatially varying index of refraction. The simplest example of such behaviour is seen by in the Twisted Nematic cell, which rotates to polarization of light 90°, as shown in Figure 5.1.

2.1.4 Maxwell's Equations

Electromagnetic waves can be accurately modelled by Maxwell's equations, show here in their macroscopic version:

$$\underline{\nabla} \cdot \underline{\mathrm{D}} = \rho_f \tag{2.6}$$

$$\underline{\nabla} \cdot \underline{\mathrm{B}} = 0 \tag{2.7}$$

$$\underline{\nabla} \times \underline{\mathrm{E}} = -\frac{\partial \underline{\mathrm{B}}}{\partial t} \tag{2.8}$$

$$\underline{\nabla} \times \underline{\mathrm{H}} = \underline{\mathrm{J}}_f + \frac{\partial \underline{\mathrm{D}}}{\partial t} \tag{2.9}$$

where $\underline{\mathrm{D}}$ is the displacement field, $\underline{\mathrm{B}}$ is the magnetic field, $\underline{\mathrm{E}}$ is the electric field, $\underline{\mathrm{H}}$ the magnetizing field, $\underline{\mathrm{J}}_f$ the free current density, and ρ_f the free charge density.

ρ_f is a measure of the density of electric charge which is not bound to an molecules, and is instead free to move within the domain.

2.1.5 Electrostatics

This thesis will work with electromagnetic waves in two distinct ways. The first is for modelling the interaction between the LC molecules and the electric field created by the electrodes. This modelling will be done using the assumption of electrostatics. The second is for modelling the optical response of the LC domain. This type of modelling will require the electromagnetic wave to be modelled, and not just the potential field. This modelling will be based on all of Maxwell's equations. For now, let us talk about electrostatics.

In order to use the electrostatic form of Maxwell's equations, we must make a few assumptions:

1. Pseudo steady-state; the electric field reaches a steady-state much faster than the molecules re-orient.
2. No current flowing through the liquid crystal material.
3. The free charge density is zero.
4. Electric field is written in terms of the gradient of potential, thus its curl is zero.

Given these simplifications, we are left with Gauss' law in terms of the displacement field:

$$\underline{\nabla} \cdot \underline{\mathrm{D}} = 0 \tag{2.10}$$

The displacement field is obtained by taking the electric field and accounting for the interaction with the material, especially the effect of polarization. Mathematically, this is written as:

$$\underline{\mathrm{D}} = \varepsilon_0 \underline{\mathrm{E}} + \underline{\mathrm{P}} \tag{2.11}$$

where ε_0 is the permittivity of free space, and $\underline{\mathrm{P}}$ is the polarization density vector.

This polarization density vector describes the magnitude and direction of permanent or induced dipoles throughout a material. For an isotropic material, it can be related to the electric field as:

$$\underline{\mathrm{P}} = \varepsilon_0 \chi \underline{\mathrm{E}} \tag{2.12}$$

where χ is electric susceptibility of the material. It represents the degree to which a material polarizes, forms dipoles, in response to an electric field. The higher the value, the stronger the dipoles. Note that $\underline{\mathrm{P}}$ is parallel to $\underline{\mathrm{E}}$ at every point in space,

Taking this equation for $\underline{\mathrm{P}}$, and substituting it back into Equation 2.11 allows us to rewrite it as follows:

$$\begin{aligned}
\underline{\mathrm{D}} &= \varepsilon_0 \underline{\mathrm{E}} + \underline{\mathrm{P}} \\
\underline{\mathrm{D}} &= \varepsilon_0 \underline{\mathrm{E}} + \varepsilon_0 \chi \underline{\mathrm{E}} \\
\underline{\mathrm{D}} &= \varepsilon_0 \underbrace{(1 + \chi)}_{\varepsilon} \underline{\mathrm{E}} \\
\underline{\mathrm{D}} &= \varepsilon_0 \varepsilon \underline{\mathrm{E}}
\end{aligned} \tag{2.13}$$

where ε is the relative permittivity of the material. Just as with $\underline{\mathrm{P}}$, $\underline{\mathrm{D}}$ is parallel to $\underline{\mathrm{E}}$ at every point in space.

A similar procedure can be done for anisotropic material, though with two important differences. First, the electric susceptibility is now a tensor:

$$\underline{\mathrm{P}} = \varepsilon_0 \underline{\underline{\chi}} \cdot \underline{\mathrm{E}} \tag{2.14}$$

where $\underline{\underline{\chi}}$ is the electric susceptibility tensor of the material.

The second difference is that unlike in the isotropic case, there is no guarantee that $\underline{\mathrm{P}}$ and $\underline{\mathrm{E}}$ are parallel. The direction of $\underline{\mathrm{P}}$ depends on the value of $\underline{\underline{\chi}}$.

Substituting Equation 2.14 into Equation 2.11 yields:

$$\begin{aligned}
\underline{\mathrm{D}} &= \varepsilon_0 \underline{\mathrm{E}} + \underline{\mathrm{P}} \\
\underline{\mathrm{D}} &= \varepsilon_0 \underline{\mathrm{E}} + \varepsilon_0 \underline{\underline{\chi}} \cdot \underline{\mathrm{E}} \\
\underline{\mathrm{D}} &= \varepsilon_0 \underbrace{\left(\underline{\underline{\delta}} + \underline{\underline{\chi}} \right)}_{\underline{\underline{\varepsilon}}} \cdot \underline{\mathrm{E}} \\
\underline{\mathrm{D}} &= \varepsilon_0 \underline{\underline{\varepsilon}} \cdot \underline{\mathrm{E}}
\end{aligned} \tag{2.15}$$

where $\underline{\underline{\varepsilon}}$ is the relative permittivity tensor.

Similarly to $\underline{\mathrm{P}}$, there is no guarantee that $\underline{\mathrm{D}}$ will be parallel to $\underline{\mathrm{E}}$.

Substituting Equation 2.15 into Equation 2.10 yields:

$$\underline{\nabla} \cdot \varepsilon_0 \underline{\underline{\varepsilon}} \cdot \underline{\mathrm{E}} = 0 \tag{2.16}$$

Since we are interested in the applied potential at the electrodes, the equation is re-written in terms of electric potential as:

$$\underline{\nabla} \cdot \varepsilon_0 \underline{\underline{\varepsilon}} \cdot \underline{\nabla} V = 0 \tag{2.17}$$

Finally, cleaning up the equation and rewriting it with tensor notation:

$$\partial_i \varepsilon_{ij} \partial_j V = 0 \tag{2.18}$$

2.2 Liquid Crystals

2.2.1 Properties

Liquid crystals (LCs) are a state of matter in-between crystalline solids and isotropic liquids, with properties also in-between those two phases. Crystalline solids are characterized by having long-range translational order (they form a lattice structure) and long-range orientational order (molecules tend to be oriented in the same direction). Isotropic liquids on the other hand lack both of these kinds of long-range order, instead having only short-range order. LCs are somewhere in-between these two states. Under this broad definition there exist a wide range of LCs, characterized by three major metrics: molecular shape, what governs their phase transition, and their phase (or "mesophase").

The shape of LC molecule can be generally classified as either disc-like (discotic) or rod-like (calamitic). Their molecular shape has profound impacts on both the mesophase observed and the resulting *texture*, the overall orientation of a LC domain.

LC phase transitions are affected by various thermodynamic conditions, such as temperature, concentration, and (to a lesser extent) pressure. LCs with temperature-dependent phase transitions are called thermotropic, while those with concentration-dependant transitions are called lyotropic.

In this work, the focus is on thermotropic rod-like nematic liquid crystals as they are the most commonly used type in LC lens research. Of the many thermotropic rod-like nematic LCs available, we will focus on 5CB since it is one of the most widely researched LCs, providing us with better access to the required modelling parameters.

t the low temperature extreme thermotropic LCs are in a crystalline solid phase, at the high temperature extreme they are in an isotropic liquid phase. In-between these two extremes, the LC can exist in one or more mesophases, see Figure 2.4; one of which is the nematic. The nematic phase is characterized by orientational order but no translational order.

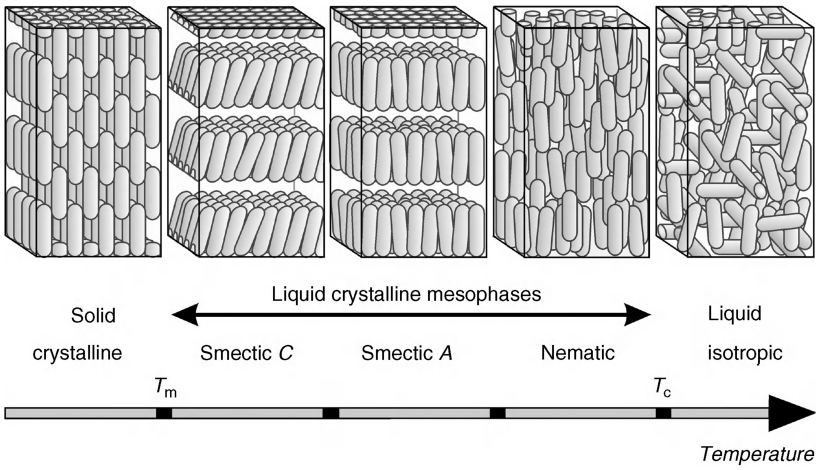

Figure 2.4: Different thermotropic LC mesophases. From [14].

LC mesophases have anisotropic physical properties due to the anisotropy of the molecules themselves. Relevant to this research is the anisotropic of their permittivity, and in turn their index of refraction. The orientation of a nematic LC at a point in space is shown in Figure 2.5 with the permittivity values labelled. Perpendicular and parallel are with

respect to the long axis of the LC[1]. When measured perpendicular to the long axis, the permittivity value is the same regardless of direction along the x-z plane. Therefore, uniaxial LCs have only 2 permittivity values.

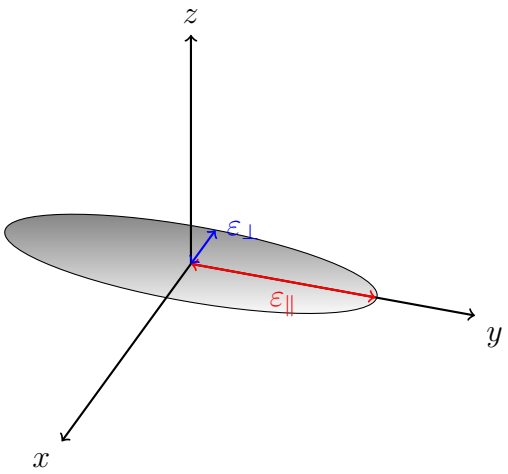

Figure 2.5: Uniaxial LC ellipsoid with parallel and perpendicular permittivity values labelled. After [8].

2.2.2 Defects

An important phenomena present in LCs is that of defects, or disclinations. Analogous to a dislocation in a crystalline material, a defect in a LC is a discontinuity or singularity in the orientation of the molecules. Figure 2.6 shows several different defect types; the lines shown are director streamlines where the director is tangent to the lines at every point. What can be observed visually from the figure is captured mathematically by the m value beneath each defect; beyond knowing that each defect type has a unique number, the meaning and calculation of this number is not relevant to this thesis. If the reader wishes to understand more, they are pointed to ref. [15].

Defects are important for two reasons: 1) they influence the optical response, and 2) they influence the modelling. From an optical point of view, a defect is, almost always, undesired since it will scatter light. In addition to the scattering, its presence means that

[1]Throughout this thesis reference will be made to the LC orientation at points in space, either through words or through glyphs in a figure. Such references do not describe the orientation of individual molecules at a point in space, but rather a volume and time average of molecular orientation around that point.

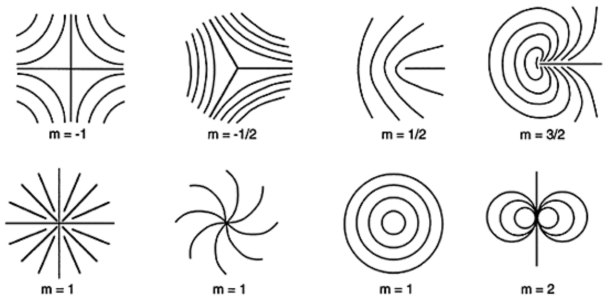

Figure 2.6: Several types of defects. Lines are director streamlines. From [16].

the rest of the texture is not what was desired. To accurately model a defect, a very fine mesh must be used. This raises feasibility concerns; the domains being modelled usually has lengths on the order of millimetres if not centimetres, but the defect area will require a mesh with resolution on the order of nanometers.

Due to these disparate length scales, adaptive mesh refinement must be used in order for the problem to be computationally tractable [17]. Thus modelling can start with a relative coarse mesh and iteratively refining only around where defects might exist[2].

2.2.3 Experimentally Observable Properties

Thus far, the discussion has focused on the texture, which is what can be controlled and what must be changed if the optical properties are not correct. Unfortunately, a major difficulty of working with liquid crystals is that the texture is extremely difficult to observe *directly*. There exist techniques for doing so [6], but their complexity and time requirement make them unfeasible for large scale engineering design. The alternative has been to observe the optical response of the LC and then back-calculate/infer the texture.

As mentioned previously, when working with anisotropic material, the material impacts the polarization of the light, and the polarization of light impacts how it interacts with the material. This behaviour is used to probe the texture of the LC through a technique called cross-polarization microscopy.

The cross-polarization microscopy setup is show in Figure 2.7.

Unpolarized light passes through a linear-polarization filter, called the polarizer. This linearly polarized light passes through the sample, where the polarization may be affected

[2]This can be estimated with a metric like the degree of biaxiality [18] or a local error estimate [17].

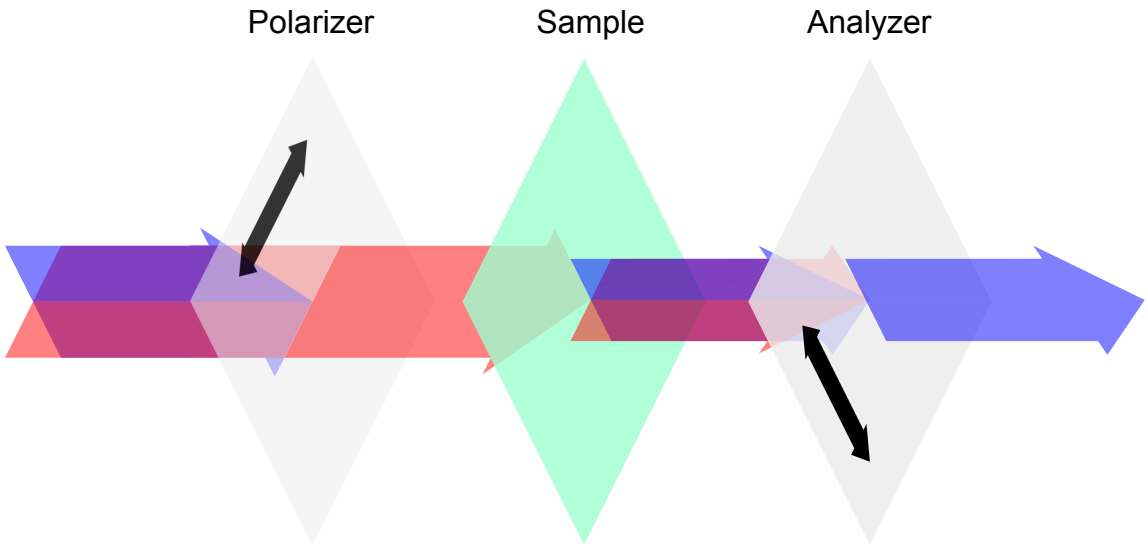

Figure 2.7: Cross-polarization microscopy with an optically active sample.

based on the local texture. The resulting light then reaches another linear-polarization filter, the analyzer, which is perpendicular to the polarizer. Any light that passes through the analyzer is then visible.

This experimental setup creates an image made up of bright and dark regions; bright regions have rotated the polarization, allowing it to pass through the analyzer, the brighter the region the closer the rotation is to $\pm 90°$. Dark regions conversely represent areas where the polarization has been relatively unaffected. By changing the angle between the sample and the polarizer, as well as the angle between polarizer and analyzer, further information can be gained about the sample.

2.2.4 Applications

Despite the difficulty of developing technology using LCs, their anisotropic nature and resulting interaction with light has turned them into an essential part of the economy through their biggest application: the liquid crystal display (LCD)[3].

LCD technology is based on the same ideas as cross-polarization microscopy: change the polarization of light in order to allow it or stop it from passing through the second

[3]For starters, the rise and current ubiquity of cell phones would not have been possible without them; what would have replaced them, a CRT-based cellphone?

polarizing filter. The brightness is controlled by the applied voltage. The implementation and materials have advanced over the decades, but all LCDs create pixels by using LC shutters. Polarized light enters the LC, the polarization is changed based on the target brightness, and then it passes through a second polarizer.

Two popular LCD designs are the Twist-Nematic (TN) cell and the In-Plane Switching (IPS) cell. The TN cell is the older of the two technologies, and therefore much simpler. While the TN cell is simple to construct, its optical properties leave room for improvements, one specific area is their poor viewing angles [19]. The IPS cell addresses this and other issues. These two LCD cells will be explored in greater detail in section 5.1, but for now let us move on to the application of LCs most relevant to this thesis: lenses.

2.3 Lenses

Lenses are a physical tool which have been employed for thousands of years to uses ranging from starting fires, enlarging reading material, correcting vision problems, microscopes, cameras, and a slew of others. For the sake of readability, "lens element" will be used to these individual lens elements and "lens" to refer to the entire optical system made up of one or more lens elements

2.3.1 How Lenses Work

Lenses operate by taking advantage of refraction, as described by Snell's law in Equation 2.1. Of the four variables in Snell's law, the angle of incidence and index of refraction of the lens material are design parameters for a lens; where the index of refraction of the environment is not under our control, and the angle of refraction is what we are trying to influence (the dependent variable). Conventional lenses are manufactured by grinding the glass substrate in order to create a spatially varying incident angle which will converge or diverge parallel light rays; an example of each is shown in Figure 2.8. The downside of this approach is that, once manufactured, that optical properties of the lens element are fixed.

2.3.2 Types of Conventional Lenses

A brief overview of the most common broad category of conventional lenses will be provided below. This overview is included since LC based adaptive lenses attempt to recreate

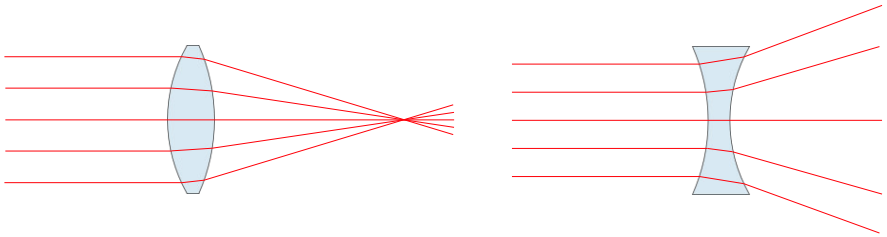

(a) (b)

Figure 2.8: Two conventional lenses, (a) a converging lens, (b) a diverging lens. After [20, 21].

these lens types, and each category poses its own unique manufacturing and/or modelling challenges.

Spherical

A spherical lens element is the most common shape and is most familiar in everyday use. They are referred to as spherical since their curved surfaces are sections of spheres, thus the angle of incidence changes as a function of radial distance. This causes light that enter the lens element to be converged to a point or broadened out uniformly.

Cylindrical

Like a spherical lens element, a cylindrical lens element gets its name from its surface curvature, which in this case is that of a cylinder. The angle of incidence for a cylindrical lens element changes only in one direction, allowing it to converge or diverge light in one direction. Thus a cylindrical lens element will converge light to a line (rather than a point) or will diverge light in only one direction.

Aspherical

The broad category of aspherical lenses refers to all lens elements with a surface curvature that is not based on sphere. An example of such lens elements is show in Figure 2.9, where

the third and forth elements from the right are aspherical. Aspherical lens elements are used in order to decrease the aberrations, the size, and/or the number of lens elements in a lens [22]. Despite these significant benefits, many ground-glass lenses employ at most 1–2 aspherical elements, if any, due to the difficulties associated with grinding such surfaces [10]. Conversely, moulded lens elements, common for small lenses such as cellphones, are commonly aspherical since the cost and difficulty in producing them is essentially the same as for spherical ones [22].

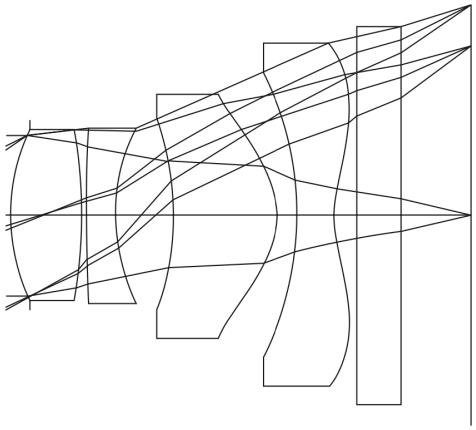

Figure 2.9: Small lens employing multiple aspherical lens elements. From [22].

Fresnel

A Fresnel lens is a variation of a spherical, cylindrical, or aspherical lens which allows it to be manufactured more compactly. A comparison of a regular spherical lens and its Fresnel version is show in Figure 2.10. The optical properties of a Fresnel lens will always be lower than its less compact version due to the diffraction occurring at the sharp corners.

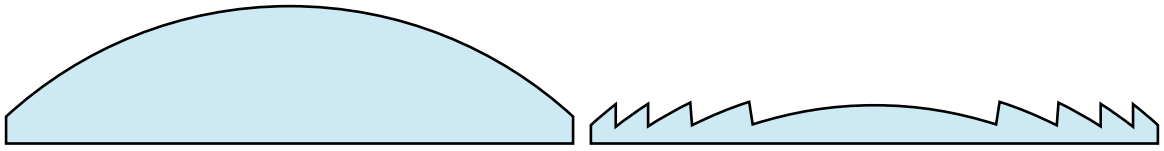

Figure 2.10: A spherical lens (right) and the equivalent Fresnel lens (left). From [23].

Gradient-Index

While most conventional lenses have a fixed index of refraction, some special purpose lens elements have a spatially varying index of refraction. These lens elements are referred to as gradient-index (GRIN) lens elements. The advantage of these lens elements is that they can have flat surfaces. The downside of GRIN lens elements is that they are harder to manufacture and, like all conventional lenses, once they have been manufactured, their optical properties cannot be changed. GRIN lens elements are common in man-made applications where the ability to have flat surfaces is beneficial, such as in fibre optic connections and photocopiers. GRIN lenses are also found in nature; many species, humans included, have GRIN lenses inside their eyes [24].

2.3.3 Types of Adaptive Lenses

Adaptive lens elements are a class of lens elements whose focal length and optical properties can be dynamically adjusted after being manufactured.

By being able to change their focal length, adaptive lens elements allow for focusing and zooming without needing to move elements relative to one another. This lack of moving parts leads to more compact and more reliable designs. Most importantly, adaptive lens elements are capable of addressing problems that cannot be solved by conventional lenses. For example, consider bifocal (or progressive) lenses and the ever increasing number of cameras on cell phones, both a direct result of the space constraints and the fact that conventional lenses cannot change their focal length.

To demonstrate the ability of such adaptive lens elements, consider Figure 2.11. When discussing an adaptive lens' ability change focal length, it is not just within a narrow range and limited to either converging or diverging light, but rather their focal length can be changed over a wide range. Figure 2.11 shows the same adaptive lens operating as both a converging and a diverging lens. To achieve the same result with conventional lenses it would require a lens with multiple elements which moved relative to one another.

There are a wide range of technological approaches proposed for adaptive lensing. This thesis focuses solely on LC based adaptive lenses; for a broader overview of several types of adaptive lens elements see ref. [4].

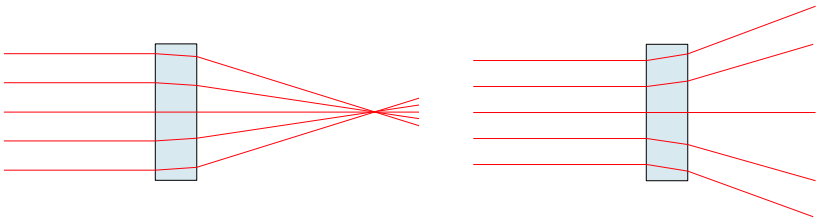

(a) (b)

Figure 2.11: An adaptive lens in two configurations: (a) A converging lens, (b) A diverging lens. After [20, 21].

Liquid Crystal Adaptive Lenses — LCALs

Unlike shape-changing lenses, liquid crystal adaptive lenses (LCALs) have no moving parts and their shape remains fixed while still having tuneable optical properties. For example, Figure 2.12 shows a LCAL in three operating models: focusing light, steering light, and letting light pass through without doing either. Additionally, LCAL can leverage decade of research, industrial experience, and existing manufacturing processes from the LCD and LC industry.

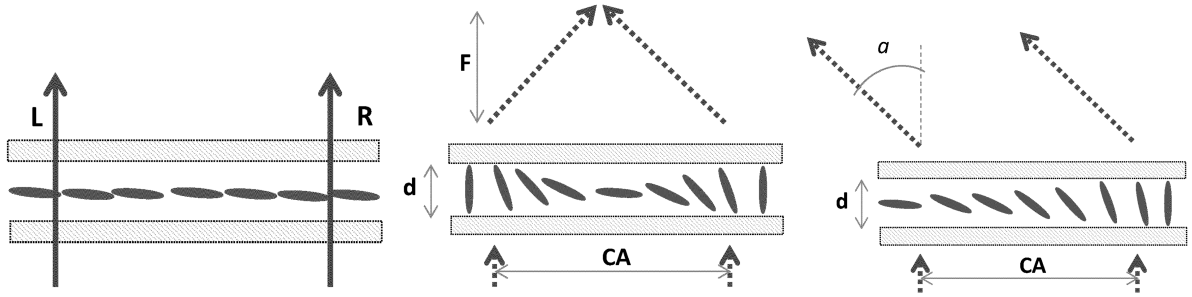

(a) (b) (c)

Figure 2.12: A LCAL in multiple modes: (a) Turned off, (b) Converging Lens, (c) Beam Steering. From [25].

LCALs change their optical properties by changing their texture in response to applied fields, rather than mechanical deformation. This can include electric and magnetic fields as well as intense light and ultrasonic waves, as will be discussed further in chapter 3.

Through precise control of an applied field, a LC texture with a spatially varying index of refraction, equivalent to a GRIN lens, can be created, see Figure 2.13. Additionally, by changing the applied field, the index of refraction will change, unlike in a regular GRIN lens. The same anisotropy that causes a net torque on the molecules in an electric field also causes light to refract to different degrees.

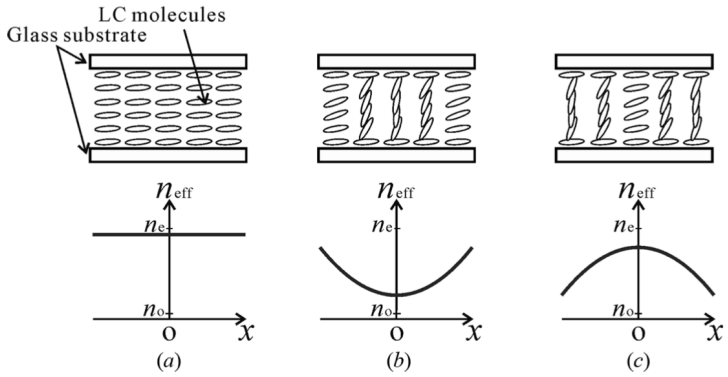

Figure 2.13: Index of Refraction Distribution in a LCAL: (a) Lens off, (b) Diverging Lens, (c) Converging Lens. From [26].

The biggest challenge of working with LCALs is the same as for LCs in general: it is not practical to directly observe the texture experimentally, thus indirect measurements and models must be relied upon. Unfortunately, these models are computationally intensive and difficult to work with due to their highly non-linear and inherent multiphysics nature. Hence, a large portion of published LCAL papers focus exclusively on experimental work.

The anisotropic properties of LCs also pose a design challenge; it results in most LCALs having some degree of polarization dependence. That is, they will affect incoming light differently based on its polarization. In display applications, this was not a significant issue since a polarized light source can be used. Unfortunately, for most lensing applications it is vital that the lenses be capable of focusing unpolarized light.

2.3.4 Lens Design History

When looking at real-life applications, most lenses contain more than one lens element. The major use-cases for single-element lenses are very simple and highly constrained, such as eye glasses. The majority of applications require lenses made up of several lens elements

to meet many requirements. These include focusing at various distances, "zooming" in and out, flattening the focal plane[4], and minimizing aberration.

An optical aberration refers to any of a large set of optical imperfections that cause light to not focus at a point. Some common aberrations are:

- **Spherical aberrations:** observable as a soft glow in the image Cause by spherical lenses whose focal length varies as a function of radial distance [11].
- **Chromatic aberrations:** observable as red, green, blue, or magenta highlights around edges. Causes by lens materials for which the index of refraction varies for different wavelengths of light [10].
- **Coma:** observable as point sources close to the image's edge have a comet-like tail. Caused by angled incoming rays being focused to different points [10].

Early lens design was performed entirely by hand, limiting lenses to simple designs. The Cooke triplet, shown Figure 2.14, is one such design from 1893, and is considered one of the most important designs in the field [1].

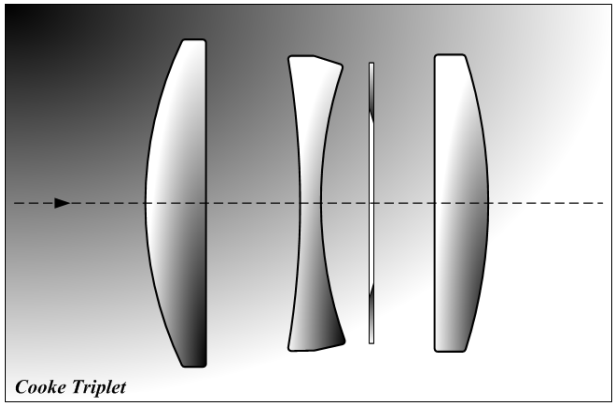

Figure 2.14: An example of a late 19th century lens, the Cooke triplet. From [27].

However, lens requirements have advanced significantly since 1893; for example see Figure 2.15.

[4]The focal "plane" is plane parallel to the front of a lens where every point on the plane is perfectly in focus. "Plane" is in quotation marks since it is a flat surface only in theory. In practice, focal "planes" have curvature.

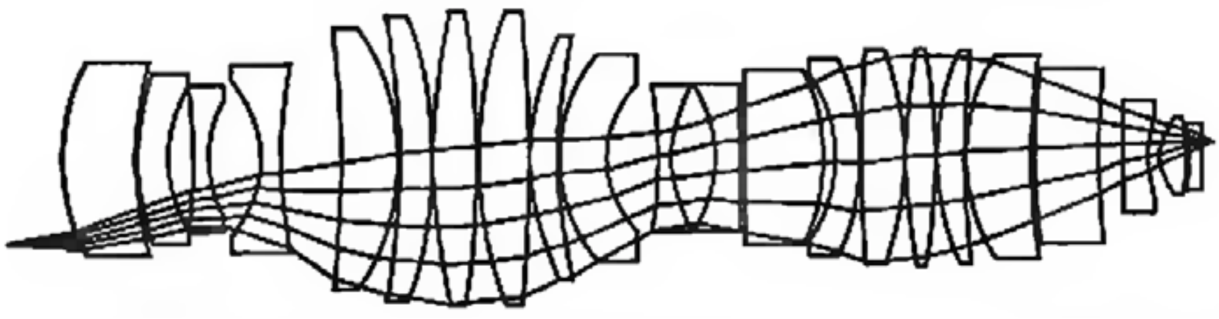

Figure 2.15: An example of a late 20th century lens made using computer aided design. From [28].

These higher demands, and the subsequent higher element count, were not met using the hand calculations of 1893. As with most other engineering fields, the introduction of computers and software tools have revolutionized the lens design process. Modern lens design is performed using specialty software, such as ZEMAX, CODE V, SYNOPSIS, and OSLO. It allows engineers to generate lens designs by performing non-linear optimization on the equations defining the system [29] . Such optimization takes into account deign considerations such as the number of elements, lens element curvatures, lens element thicknesses, and optical aberrations. The role of the optical engineer is to identify the design constraints, setup the cost function, and evaluate the many different results that the software will provide, each representing a local minimum of equal mathematical merit[5].

All of this is possible since conventional lenses are relatively-simple to model; the curvature is easily specified using mathematical functions, and optical properties are modelled using ray tracing. Such software does not support adaptive lenses; rather than being able to impose a curvature using a predefined mathematical function, the surface curvature or index of refraction distribution in an adaptive lens must be obtained from multiphysics models.

2.4 LC Modelling

For LCALs, the theoretical model used must account for relatively large scales, up to tens of centimetres. This lengths scale rules out the use of molecular dynamic models as they

[5] Another, even more important role (to quote a modern lens design textbook) is to manage expectations, "if the customer wants to violate a law of optics, you might persuade him to adopt a more reasonable set of goals." [30].

would be computationally infeasible. Instead, a continuum model must be used.

For LCs, these model fall into one of two categories: hydrostatic, and hydrodynamic. This thesis will focus on models that make the hydrostatic approximation, i.e. no flow. Since hydrodynamic model can be obtained by augmenting the hydrostatic model [31], the extension of the model to a hydrodynamic model is possible in future work.

Two hydrostatic models will be discussed in this section: one based on Frank-Oseen theory, and another based on Landau-de Gennes theory. The model based on Frank-Oseen is less computationally intensive, but it does not capture all of the required physical behaviour. In contrast, the model based on Landau-de Gennes theory addresses these shortcomings, but at the cost of higher computational costs and difficult to obtain parameters. However, before discussing either of these theories, we will first go over the mathematical representations of orientational ordering in the nematic phase.

2.4.1 Order Parameters

Scalar Order Parameter

The first representation is based on a vector and a scalar order parameter. The vector, referred to as the "director" and shown as n_i in equations, represents the average orientation of the molecules around some point in space, with their thermal fluctuations averaged out. The models using it, are invariant under inversions of n_i; that is, n_i and $-n_i$ represent the same configuration and free-energy contribution. Since it is an average, the orientation of individual molecules will have some deviation from it. In this representation, the nematic is assuming to be uniaxial, thus this deviation is only with respect to the azimuthal angle θ. Figure 2.16(a) shows this angle, θ, between the director, n_i, and the orientation of a particular molecule, u_i.

These angles θ are random distributed around a mean of 0, by definition of n_i. The degree to which θ varies is dependant on the conditions of the nematic; Figure 2.16(b) shows two cases, one with more variation (lower degree of ordering) in dashed-black and one with less variation (higher degree of ordering) in solid-red. In order to be of use to the model, the insight seen visually in the probability distributions must be captured mathematically. This is done through the scalar, or uniaxial, order parameter, S, defined as:

$$\begin{aligned} S &= \int_0^{\pi} f(\theta) \frac{1}{2} \left(3\cos^2\theta - 1\right) d\theta \\ &= \frac{1}{2} \left\langle 3\cos^2\theta - 1 \right\rangle \end{aligned} \tag{2.19}$$

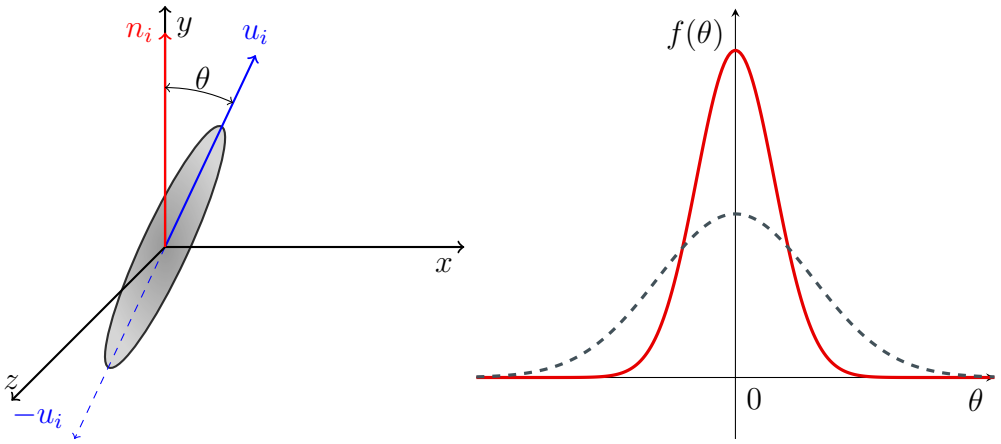

Figure 2.16: (a) Molecular orientation, where $\hat{n}$ is the director and $\hat{u}$ is orientation of a particular molecule, (b) orientation distribution corresponding to low (dashed-black) and high (solid-red) degree of ordering. From [8].

Aside from the uniaxial assumption, this representation for the LC texture has another drawback: it does not handle defects. Recalling Figure 2.6, n_i is degenerate in each defect. This degeneracy and discontinuous change in the director causes problems for numerical stability.

Tensor Order Parameter

Using n_i and S to model liquid crystals has several shortcomings that are intrinsic to the vector representation. An improved order parameter which addresses these issues is the alignment tensor, Q_{ij} [32]. While n_i changed discontinuously around a defect, Q_{ij} changes smoothly, and while the director model assumes uniaxial behaviour, the tensor model captures biaxiality. The ability to account for biaxiality increases the physicality of the model since biaxiality occurs around areas of interest such as defects and surfaces. Around the defect, biaxiality increases due to the discontinuous change in molecular orientation. Around a surface, biaxiality increases because the molecules are physically unable to vibrate as freely in the direction of the surface.

To begin the derivation, we again look at a small region of LC material where the orientation of each molecule is represented by u_i, as shown in Figure 2.17(a). Unlike in the director representation, rotational symmetry around the $\hat{y}$ is not assumed. Projecting u_i onto the unit sphere, we define $f(u_i)$ as the probability density function of u_i. Figure 2.17(b) shows two different equal-probability contours. The blue curve depicts the

uniaxial case, where rotational symmetry around $\hat{y}$ is present. The red curve depicts the biaxial case, where that rotational symmetry is not present and the molecules have a preference for one direction ($\hat{z}$) over the other ($\hat{x}$).

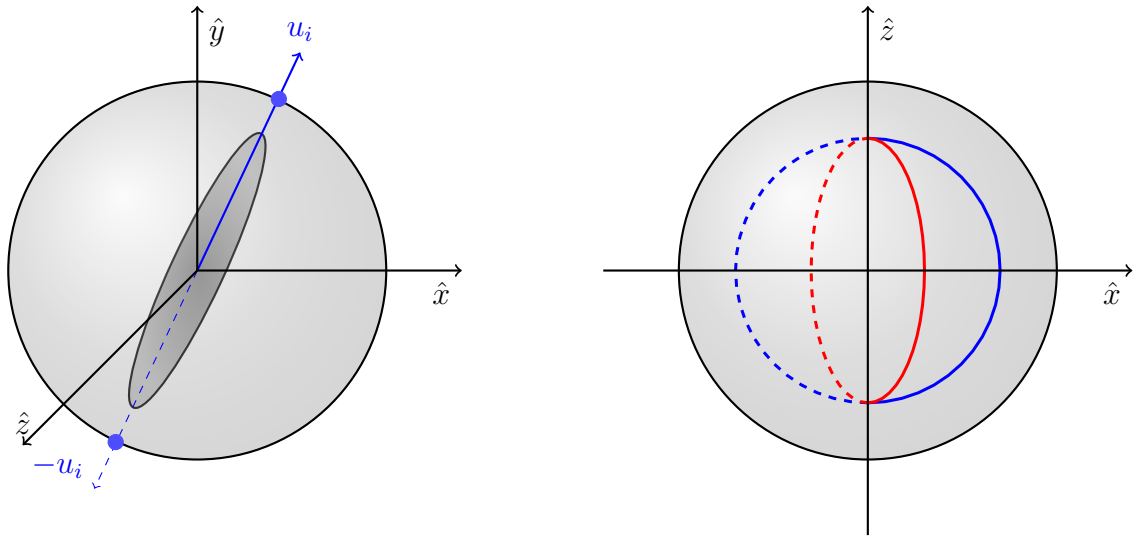

(a) (b)

Figure 2.17: (a) Molecular axis point to position on unit sphere, (b) equal probability contours for uniaxial alignment (blue) and biaxial alignment (red). From [8].

Taking the first and second moments of this distribution yields:

$$\int u_i f(u_i) \mathrm{dS} = 0 \tag{2.20}$$

$$\int u_i u_j f(u_i) \mathrm{dS} = M_{ij} \tag{2.21}$$

The first moment is zero since $f(u_i) = f(-u_i)$, as can be seen from Figure 2.17(a). The second moment produces a symmetric rank-2 tensor.

The Q-tensor is defined as the deviation of this second moment, M_{ij}, from the second moment of the isotropic state. Thus, the next step is to calculate the moment for isotropic

phase:

$$\begin{aligned} M_{ij}^{(iso)} &= \int u_i u_j f^{(iso)}(u_i) \mathrm{dS} \\ &= \int u_i u_j \frac{1}{4\pi} \mathrm{dS} \\ &= \frac{1}{4\pi} \int u_i u_j \mathrm{dS} \\ M_{ij}^{(iso)} &= \frac{1}{3}\delta_{ij} \end{aligned} \tag{2.22}$$

Combining the two moments:

$$\begin{aligned} Q_{ij} &= M_{ij} - M_{ij}^{(iso)} \\ Q_{ij} &= M_{ij} - \frac{1}{3}\delta_{ij} \end{aligned} \tag{2.23}$$

The alignment tensor is a symmetric-traceless rank-2 tensor. M_{ij} was symmetric, and subtracting $M_{ij}^{(iso)}$ from it removes its trace.

Since Q_{ij} is symmetric-traceless and real it will have orthonormal eigenvectors and real-valued eigenvalues. Thus, it is possible to use them as the basis onto which to Q_{ij} can be diagonalized:

$$Q_{ij} = \lambda_1 n_i n_j + \lambda_2 m_i m_j + \lambda_3 l_i l_j \tag{2.24}$$

where λ_1, λ_2, and λ_3, are the eigenvalues in decreasing size, and n_i, m_i, and l_i are the corresponding eigenvectors.

This diagonalization can, with significant effort, be rewritten as:

$$Q_{ij} = S\left(n_i n_j - \frac{1}{3}\delta_{ij}\right) + P(m_i m_j - l_i l_j) \tag{2.25}$$

where S is the degree of uniaxial alignment, and P is degree of biaxial alignment. These values are related back to the eigenvalues as:

$$S = \frac{2}{3}\lambda_1 \tag{2.26}$$

$$P = \frac{\lambda_2 - \lambda_3}{2} \tag{2.27}$$

As discussed previously, S quantifies the degree of uniaxial alignment. Visually, the value of S is directly related to the size of the contours in Figure 2.17(b); the larger the value, the large the circle/ellipse. P quantifies the degree of biaxial alignment. It can be visually though of as representing the ratio between the semi-major and semi-minor axes of the ellipse; the greater the value the more elliptical the equal probability contours.

2.4.2 Frank-Oseen Theory

Frank-Oseen theory is a continuum theory originating in work done by Oseen which was reformulated and expanded upon by Frank [33]. Oseen's work sets up the foundations of liquid crystal elasticity theory, treating the free-energy contributions of changes in director orientation as one would the energy contribution of the elastic deformation of a spring. The lowest energy state for a nematic phase is the fully aligned state, and any deviations from this state are given an associated free-energy contribution. Expanding this free-energy representation up to second order and rearranging yields [34]:

$$f_f = \underbrace{\frac{1}{2}k_{11}(\underline{\nabla}\cdot\underline{\mathrm{n}})^2}_{\text{splay}} + \underbrace{\frac{1}{2}k_{22}(\underline{\mathrm{n}}\cdot\underline{\nabla}\times\underline{\mathrm{n}})^2}_{\text{twist}} + \underbrace{\frac{1}{2}k_{33}(\underline{\mathrm{n}}\times\underline{\nabla}\times\underline{\mathrm{n}})^2}_{\text{bend}} \\ \underbrace{-\frac{1}{2}\left(k_{22}+k_{24}\right)\underline{\nabla}\cdot(\underline{\mathrm{n}}(\underline{\nabla}\cdot\underline{\mathrm{n}})+\underline{\mathrm{n}}\times\underline{\nabla}\times\underline{\mathrm{n}}))}_{\text{saddle-splay}} \tag{2.28}$$

where k_{11}, k_{22}, k_{33}, and k_{24} are the energy constants associated with splay, twist, bend, and saddle-splay deformations; each is visually represented in Figure 2.18. Note that each term in this equation has two instances of n_i multiplied together, thus it will be invariant under sign inversions of n_i.

While the free-energy terms are easy to interpret, see Figure 2.18, it suffers from several limitations:

- Being based on the the director representation, it cannot properly model defects or defect formations.
- Using only n_i and S, the model is unable to capture biaxiality.
- The value of S is assumed to be spatially invariant. Thus the model cannot capture spatial variations in thermodynamic bulk free-energy associated with a spatially varying orientation strength.

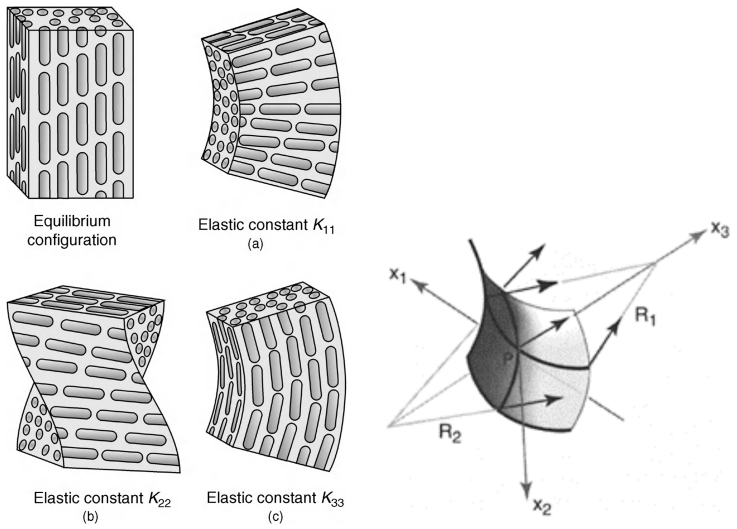

(a) (b)

Figure 2.18: Visual representation of the Frank-Oseen constants. (a) k_{11}, k_{22}, and k_{33} from [14], (b) k_{24} from [16].

The model is often further simplified in order to speed up computation. The most common of these simplifications is omitting the saddle-splay contribution. Since that term can be rewritten as a surface integral, it can be justifiably omitted when other surface forces, such as strong anchoring, dominate the surface, or when bulk energy contributions dominate [35]. This approximation is often used in conjunction with using Dirichlet boundary conditions to apply surface anchoring, an unrealistic approximation which will be discussed in section 2.4.3. Another common approximation is assuming that the remaining 3 constants are the same, i.e. $k_{11} = k_{22} = k_{33}$. And finally, there is the one constant approximation; assuming that $k_{22} = k_{33} = k_{24} = 0$, simplifying Equation 2.28 to:

$$f_f = \frac{1}{2} k_{11} (\underline{\nabla} \cdot \underline{\mathrm{n}})^2 \tag{2.29}$$

While these approximations reduce the computational complexity of modelling, the already limited modelling capabilities of the director approach are further reduced. Such an approach cannot be taken when trying to create a general model.

2.4.3 Landau-de Gennes Theory

The Landu-de Gennes theory is the second continuum hydrostatic model being explored in this thesis. It is based on Pierre-Gilles de Gennes' model for the nematic-isotropic phase transition which was extended by Lev Landau through a truncated power-series expansion with respect to a new order parameter, Q_{ij} [34]. It allows for the prediction of LC behaviour that past models could not capture, such as the formation of topological defects, biaxiality, spatial variations in degree of alignment, and variation of LC elasticity, and dynamics.

Bulk Free-Energy

As mentioned earlier, Landau-de Gennes theory is based on a free-energy expansion in terms of Q_{ij}. The terms in the expansion written only in terms of Q_{ij} are grouped together and taken to represent the bulk free-energy density:

$$f_{bulk} = f_{iso} + \frac{1}{2}a_0 \left(T - T^*_{NI}\right) Q_{ij}Q_{ji} - \frac{1}{3}bQ_{ij}Q_{jk}Q_{ki} + \frac{1}{4}c \left(Q_{ij}Q_{ji}\right)^2 \tag{2.30}$$

where f_{iso} is the free-energy density of the isotropic state; a_0, b, and c are temperature independent constants related to the phase transition of a particular LC; T is the temperature of the system; and T^*_{NI} is the supercooling temperature, the temperature at which the isotropic state is no longer stable, slightly below the nematic-isotropic transition temperature T_{NI}.

Elastic Free-Energy

The gradient terms in that expansion are taken together to represent the energy associated with elastic deformation. These terms assign a free-energy contribution to different gradients of the director within the material:

$$\begin{aligned} f_{elas} = \frac{1}{2}L_1 \left(\partial_i Q_{jk} \partial_i Q_{kj}\right) + \frac{1}{2}L_2 \left(\partial_i Q_{ij} \partial_k Q_{kj}\right) + \frac{1}{2}L_3 \left(Q_{ij} \partial_i Q_{kl} \partial_j Q_{kl}\right) \\ + \frac{1}{2}L_{24} \left(\partial_k Q_{ij} \partial_j Q_{ik}\right) \end{aligned} \tag{2.31}$$

Unlike in Frank-Oseen theory, where each constant is associated with a specific type of deformation (splay, twist, bend, and saddle-splay), the Landau-de Gennes elastic constants do not have a clear interpretation. Because of this, they are difficult to measure experimentally. Their values are obtained by performing experiments where the Frank-Oseen and

Landau-de Gennes theory as equally valid, i.e. uniaxial alignment with spatially uniform S. Under these conditions, the elastic constant from these two theories can be related as [36]:

$$L_1 = \frac{1}{6S_{eq}^2}\left(k_{33} - k_{11} + 3k_{22}\right) \tag{2.32}$$

$$L_2 = \frac{1}{S_{eq}^2}\left(k_{11} - k_{22} - k_{24}\right) \tag{2.33}$$

$$L_3 = \frac{1}{2S_{eq}^3}\left(k_{33} - k_{11}\right) \tag{2.34}$$

$$L_{24} = \frac{1}{S_{eq}^2}\left(k_{24}\right) \tag{2.35}$$

where S_{eq} is the equilibrium uniaxial order parameter calculated under the conditions described above.

To obtain S_{eq}, one introduces the uniaxial decomposition for Q_{ij} into Equation 2.30 to yield:

$$f_{bulk}(S) = \frac{1}{3}a_0\left(T - T_{NI}^*\right)S^2 + \frac{2}{27}bS^3 + \frac{1}{9}cS^4 \tag{2.36}$$

The above equation is then minimized in terms of S to yield:

$$S_{eq} = \frac{b}{4c}\left(1 + \sqrt{1 - 24\frac{a_0 c\left(T - T_{NI}^*\right)}{b^2}}\right) \tag{2.37}$$

Electric Free-Energy

The free-energy contribution associated with an electric field as derived in ref. [8] is :

$$f_{elec} = \frac{\varepsilon_0}{2}\underbrace{\left(\frac{\varepsilon_\parallel + 2\varepsilon_\perp}{3}\delta_{ij} + \left(\varepsilon_\parallel - \varepsilon_\perp\right)Q_{ij}\right)}_{\varepsilon_{ij}}\partial_j V \partial_i V \tag{2.38}$$

where $\varepsilon_\parallel$ the relative permittivity parallel to the long axis of the molecule, and $\varepsilon_\perp$ the relative permittivity perpendicular to the long axis of the molecule.

Of note is the term $\varepsilon_\parallel - \varepsilon_\perp$, which is the contribution associated with the anisotropy of the material. While the first term, the isotropic contribution, is always positive, the sign of

this anisotropic contribution depends on the nematic material. Thus, in order to minimize this free-energy, a molecule with a positive permittivity anisotropy will tend to align its long axis, parallel to the electric field lines, while a molecule with a negative permittivity anisotropy with tend to align itself perpendicular to the electric field lines.

We have chosen to work with the electric potential field V rather than the electric field E_i. This is for convenience since our electrode boundary conditions will be in terms of the applied electric potential.

A similar equation could be derived and included for the magnetic field, but it has been omitted from this model as we will be focusing exclusively on stationary applied electric fields.

Surface-Free Energy

The last term to discuss is associated with the orientation of the molecules at the surface of the LC domain, the surface anchoring. Physically, this anchoring is imposed through the use of surfactants, physical rubbing, or polymer brushes. Numerically, this anchoring can be modelled using either Dirichlet boundary conditions, or a free-energy contribution term. The use of a Dirichlet boundary condition represents infinitely strong anchoring at the surface. A more generalizable, and physically accurate, way of modelling the anchoring at the surface is through a free-energy term. Where a Dirichlet boundary condition forces a particular orientation at the surface, this anchoring free-energy defines a preferred orientation and allows the molecules to re-orient in response to other competing forces. This approach is especially more accurate when weak anchoring is present, i.e. very little energy is needed to re-orient the molecules. It allows for such things as the relaxation of a defect out of the domain through the surface, something not possible if the orientation of the surface molecules is fixed.

The simplest anchoring model to use is Rapini-Popualar [37]. It was originally proposed using the director representation for models based on Frank-Oseen theory, but it has been rewritten for a Q tensor representation as [38]:

$$f_{surf} = \frac{1}{2}\alpha \left(Q_{ij} - Q^s_{ij}\right)^2 \tag{2.39}$$

where α is the anchoring strength and Q^s_{ij} is the preferred anchoring on the surface, obtained using Equation 2.25 using $S = S_{eq}$ and $n_i = h_i$ where h_i is the preferred direction (e.g. surface normal for homeotropic anchoring). In the limit of $\alpha \to \infty$ the anchoring becomes strong, essentially a Dirichlet boundary condition.

Total-Free Energy

Combining Equation 2.30, 2.31, 2.38, and 2.39 and integrating over the entire domain yields:

$$
\begin{aligned}
F = & \iiint_{\Omega} f_{vol}\,\mathrm{d}\Omega + \iint_{\Gamma} f_{surf}\,\mathrm{d}\Gamma \\
= & \iiint_{\Omega} [f_{bulk} + f_{elas} + f_{elec}]\,\mathrm{d}\Omega + \iint_{\Gamma} f_{surf}\,\mathrm{d}\Gamma \\
= & \iiint_{\Omega} \Bigg[\frac{1}{2} a_0 (T - T_{ni}) Q_{ij} Q_{ji} - \frac{1}{3} b\, Q_{ij} Q_{jk} Q_{ki} + \frac{1}{4} c\, (Q_{ij} Q_{jk})^2 \\
& \qquad + \frac{1}{2} L_1 (\partial_i Q_{jk} \partial_i Q_{kj}) + \frac{1}{2} L_2 (\partial_i Q_{ij} \partial_k Q_{kj}) \\
& \qquad + \frac{1}{2} L_3 (Q_{ij} \partial_i Q_{kl} \partial_j Q_{kl}) + \frac{1}{2} L_4 (\partial_k Q_{ij} \partial_j Q_{ik}) \qquad (2.40) \\
& \qquad + \frac{\varepsilon_0}{2} \Big(\frac{\varepsilon_{\parallel} + 2\varepsilon_{\perp}}{3} \delta_{ij} + (\varepsilon_{\parallel} - \varepsilon_{\perp}) Q_{ij} \Big) \partial_j V \partial_i V \Bigg]\,\mathrm{d}\Omega \\
& + \iint_{\Gamma} \frac{1}{2} \alpha (Q_{ij} - Q^s_{ij})^2\,\mathrm{d}\Gamma \qquad (2.41)
\end{aligned}
$$

where Ω is the entire domain, and Γ its bounding surface.

Chapter 3

Literature Review

This chapter aims to provide the reader with a brief history of liquid crystal adaptive lenses (LCALs) as well as an overview of design considerations, past modelling work, and applications being actively pursued. The field of LCALs is small compared to other applications of liquid crystals, such as LCDs, likely due to the challenges of commercialization. It has existed since the late 1970s, with the first mention of LCALs dating back to a 1977 patent for Berramen and Bell Labs [39]. This was followed by a 1979 paper from Susumu Sato [40] and a 1981 NASA presentation by Kowel and Cleverly [41], with two subsequent papers by the pair [42, 43].

Despite the recent start and the current relatively small size, is too large to exhaustively review all past research in this chapter. For a broad and comprehensive overview the reader is directed to all of the following references [44, 45, 46, 4, 47, 48, 49]. While a great number of LC mesophases are begin investigated for lensing applications [50, 51, 52, 53, 54], this thesis will focus on the nematic phase as it is the least challenging to model and the one most commonly used in the literature for LCALs.

The design considerations covered are the different modes of control for LCALs, the different lens shapes, the shape and number of domains, different anchoring conditions, and options for achieving polarization independence. Then, the modelling implications of these design considerations will be discussed. Subsequently, previous modelling work will be examined in terms of the techniques, models used, and shortcomings. Finally, the applications covered will be in the field of medicine and consumer electronics, focusing mainly on the use of LCALs for eyes and cameras.

3.1 Design Considerations

Even with the limited focus of nematics LCALs, there exists a wide variety of lens designs. This variety in designs speaks to the very different requirements of the proposed use-cases. A LCAL used in a cellphone will prioritize response time, energy consumption, and optical quality; one used for a spotlight will prioritize high-temperature stability and aperture size.

3.1.1 Modes of Control

Some early lenses were created that did not require an external field. Instead, they had two focal lengths: one for vertical linear polarized light, and one for horizontal [40]. A polar filter was then placed in front of the lens; the rotation of the filter changed the focal length between that of the two polarization states. This kind of lens design has not been pursued further due to the downsides of its strong polarization dependence.

The majority of approaches to liquid crystal lenses are based on the control of the texture in response to an external field. Some research has looked into using ultrasonic vibrations to control alignment into lens-like configurations [55]. Such research is an exception to the norm. Most research has focused on using an electromagnetic field to control the LC lensing effect. Researchers have generally limited themselves to using either an electric field or a magnetic field rather than both, likely for simplicity. Some of the more exotic research into electromagnetic control models involves high intensity light [56]. Just as the molecules experience a net torque from the electric field created by electrodes, so too will the experience a net torque from the electric field associated with very intense light. This thesis will focus on the control of LCAL through electric field since it will allow the model to have the greatest academic and industrial relevance.

In order to prevent the migration and formation of ions in the LC, an alternating current (AC) field is used [57]. In addition to no migration, an AC field allows for an extra degree of freedom: frequency. A LCAL can be controlled by a combination of the electric potential and frequency of the applied field. Voltage control involves changing the electric potential of the applied field, thereby changing the "torque" on the molecules. Frequency control operates by taking advantage of the frequency dependence of the permittivity anisotropy; it is not constant across frequencies, and the parallel and perpendicular values change at different rates. As discussed, the permittivity anisotropy dictates the response of a molecule to an electric field. The magnitude dictates the "torque" experienced, and the sign dictates if the molecules prefers to align itself parallel or perpendicular to the field lines.

Initial designs operated solely on voltage control; the higher the potential difference, the stronger the torque on the molecules, leading to more re-orientation. A diagram of a LCAL with voltage control is shown in Figure 3.1. The electrode configuration for this LCAL allows it to function as both a converging and diverging lens, depending on the applied electric potential. This approach is simple to implement in the lab, all one needs is a variable voltage power supply. However, it is much more difficult to implement in consumer electronics that run on constant voltage batteries.

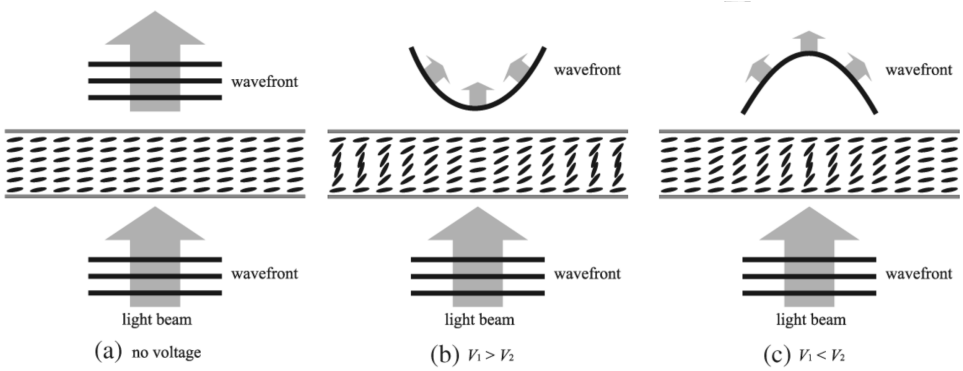

Figure 3.1: A LCAL in three different configurations: (a) lens powered off, (b) converging light, (c) diverging light. After [58].

Frequency control, in contrast, is much simpler to implement from a constant voltage power supply. This is because a square-wave AC signal can be easily created from a DC source through an approach similar to pulse width modulation. The addition of frequency control allows for improved lens performance by providing extra degrees of freedom with which to optimize lens performance. Frequency control can be performed with multiple frequencies to introduce even more degrees of freedom [59]. Low frequency signals are able to propagate across the entire aperture providing a "base" lens profile. Higher frequencies are superimposed onto this in order to make small changes to the lens profile at the periphery of the lens; the higher frequencies dissipate faster, and thus will not penetrate beyond the edges of the lens. Another approach is to combine frequency and voltage control [60, 61]. This allows for designs using so-called "dual-frequency" LCALs whose permittivity anisotropy changes sign between the two different frequencies (e.g. 50kHz vs 1kHz [61]). This allows the lens to function as both a converging and diverging lens while maintaining a simple electrode configuration; the frequency dictates if the lens is in converging or diverging mode, and the potential difference dictates the strength of the lens.

3.1.2 Lens Shapes

As shown in Figure 2.13, LCALs function as electrically-tuneable GRIN lenses; allowing the design of lenses with arbitrary index of refraction fields. Much of the published literature focuses on "spherical" and "cylindrical" LCALs, with some research on Fresnel-type index of refraction distributions. "Spherical" and "cylindrical" are in quotation marks since while the authors refer to them as spherical/cylindrical lenses they are neither of those. A spherical or a cylindrical lens have a phase profile, or an index of refraction profile, that is an arc of a circle. The LCALs being published in literature do not have such phase profiles nor are they trying to achieve them. Rather, they are being designed and compared against a parabolic profile. Most papers compare their phase profile against a parabolic one without discussing it, they merely show it in their figures. Only some papers explicitly state the their reference profile is parabolic [62, 26, 63]. This difference may seem minor, but from a lens design perspective it very much is not. A parabolic lens profile will result in a parabolic lens; free of spherical aberrations but inherently featuring coma [10]. However, for the purposes of this discussion, the terms spherical and cylindrical will be used, despite not being entirely accurate.

We shall start by looking at cylindrical LCALs, which have the simplest lens design. From a manufacturing perspective, the linear electrodes required for cylindrical LCAL designs are easily manufactured since they are the same geometry as those used in LCDs. The design features a planar thin-film LC domain with electrodes on the top and bottom; the bottom surface has a single solid electrode, while the top surface has an electrode with a rectangular hole in it. This geometry is shown in Figure 3.2.

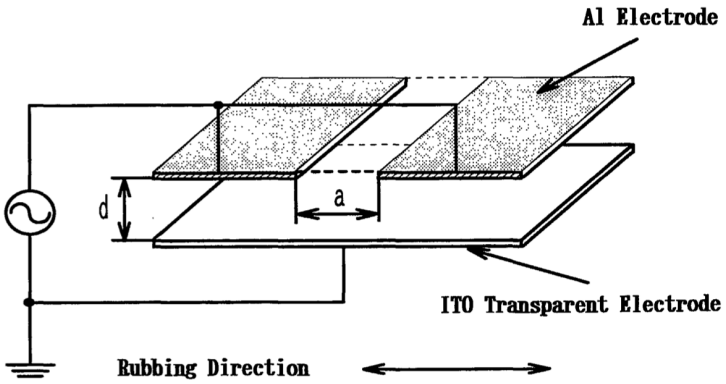

Figure 3.2: Electrode configuration for a simple cylindrical LCAL. From [64].

Compared to spherical LCALs, cylindrical LCALs have received significantly less re-

search attention (based on the number of papers published). Of the research that has been done, most focused on creating cylindrical LCALs for the purpose of focusing light to a line [64, 65, 66]. Some research, on the other hand, combined multiple cylindrical LCALs in order to produce a lens that focuses light to a point [42, 67, 68]; the first set of cylindrical LCALs focus light to a line and the second set, oriented perpendicular to the first, focused this line to a point. This approach to creating spherical LCALs will be explored in detail and modelled in chapter 6. This use of cylindrical LCALs to converge light to a point, or in the reverse process of diverging light in both direction, results in lenses of lower optical quality than what can be obtained by spherical lenses. The advantage of this approach is that such lenses can be manufactured more easily by leveraging existing LCD manufacturing expertise.

While cylindrical LCALs are able to be designed using simple linear electrodes, spherical LCALs require circular holes-patterned electrodes [69], ring electrodes [70], or a wide range of more complicated to manufacture configurations [40, 71, 72, 73, 74]. Figure 3.3 shows an example of the the hole-patterned and the spherical ring electrode configurations.

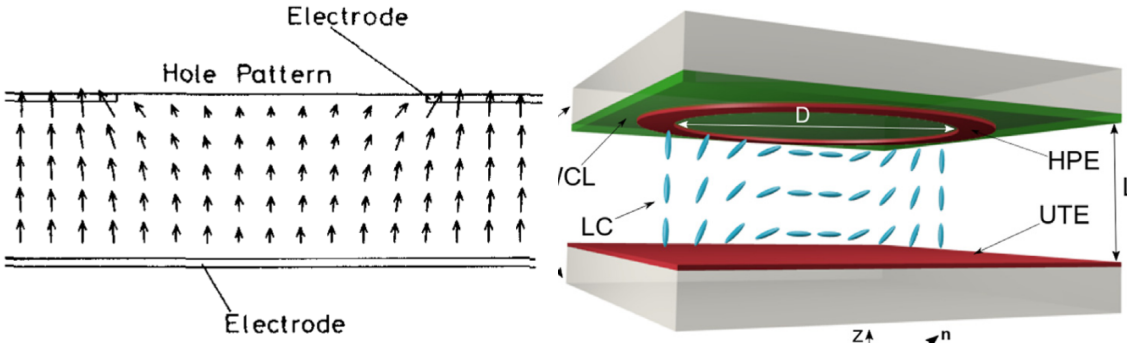

(a) (b)

Figure 3.3: Electrode configuration: (a) hole-patterned electrode from [69], (b) spherical ring electrode from [70].

Fresnel-type LCALs are desirable for three reasons: faster response times [63], thinner lenses [75], and polarization independence [76]. Where spherical LCALs could be constructed with a single ring electrode, Fresnel LCALs require anywhere from three to tens of ring electrodes as well as bus lines, the straight lines in Figure 3.4(a), to connect each ring [77, 75]. An example of the electrode structure for a Fresnel LCAL is show in Figure 3.4[1].

[1]The number of electrodes is not the same between these two lenses as they are from different papers, but the idea is the same.

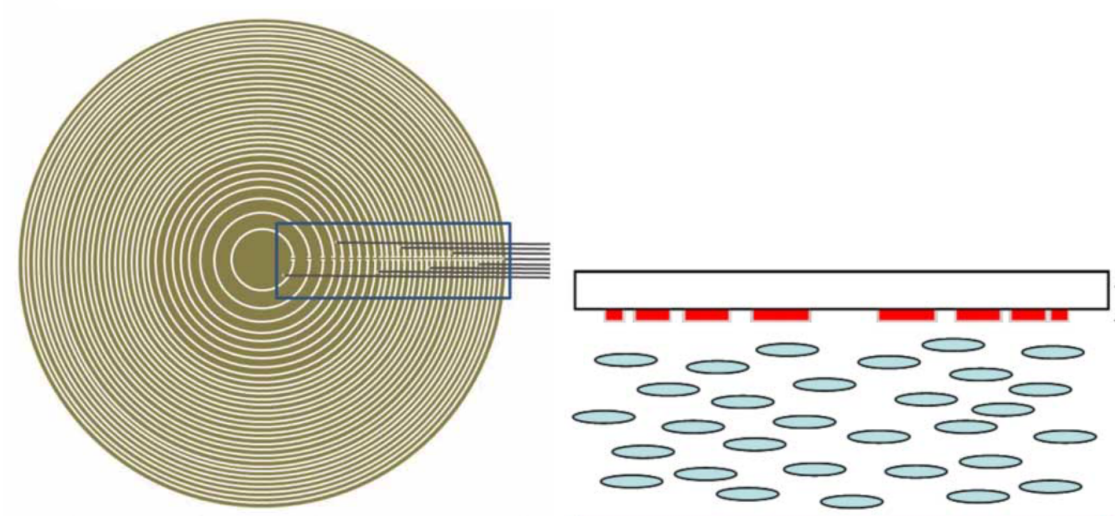

(a) (b)

Figure 3.4: Electrode configuration for a Fresnel LCALs: (a) top-down view from [75], (b) side view from [78].

3.1.3 Shape and Number of LC Domains

With their ability to spatially vary their index of refraction, LCALs do not need be designed with curved surfaces in order to function. Despite this, a handful of LCAL designs still incorporate curved surfaces because the surface curvature offers extra degrees of freedom, which could be used to improve optical performance. Sato's original paper placed the LC material between a glass plate and a conventional lens [40]. Another use of a curved surface is to create a polarization-independent microlens [79]; a spherical hole is combined with homeotropic (meaning perpendicular to the surface) anchoring to create a texture with, theoretically, rotational symmetry. This design is shown in Figure 3.5(a).

3.1.4 Polarization Independence

The polarization dependence of a LCAL is a significant design consideration and drawback of the technology. Most lensing applications, especially consumer ones, require the focusing of unpolarized light, such as given off by the sun and most artificial light sources. The simplest approach, thus far, to overcome this issue is to stack a pairs of LCALs, each of which focuses linearly polarized light, at 90° to each other [80, 81, 82, 83]. The first lens

in the pair would focus the component of incoming electric waves which are parallel to polarization its sensitive to, and the second would do the same with the other, orthogonal, linear polarization.

Other approaches include using a Fresnel lens design with planar anchoring, where the rubbing direction of the Fresnel zones alternates [76]. This effectively creates two lower order Fresnel lenses superimposed on one another, each focusing perpendicularly-linearly-polarized light.

Then there is the designs which use homeotropic anchoring, which relies on the creation of a radially symmetric texture. One such design is to use a spherically curved bottom surface, causing the LC molecules to point towards the central axis of the lens [79]. Another, is to use a LC with negative permittivity anisotropy, which turns to align its short axis with the electric field lines [84]. Both of these two designs are shown in Figure 3.5.

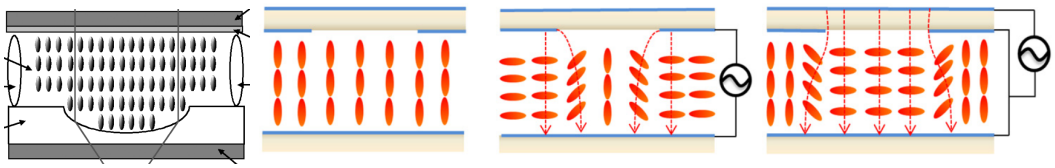

(a) (b)

Figure 3.5: Designs of polarization independent LCALs with homeotropic anchoring: (a) curved surface, from [79], (b) negative permittivity anisotropy LC, from [84].

Another approach to overcome polarization dependence is through the use of mirrors. Light passes through a LCAL and has one component focused, then it reflects off a mirror, which will flip its polarization [12]. The reflected light passes through the same lens a second time [85, 86]. The light is then sent to a sensor by use of a beam-splitter.

3.2 Consequences of LCAL Design Choices on Modelling

The design choices discussed throughout this chapter have implications on the requirements to accurately model the LCAL.

The first design choice discussed was the mode of control. Looking at only the electric field, the choice of voltage or frequency control dictates the kind of model that has to be

used. Voltage control is the least complex approach to model since a real-valued permittivity tensor can be used. Frequency control is more challenging since the electric field model would need to take into account dissipation, represented by a complex permittivity tensor, and multiple frequencies.

Next, was the choice of lens type (cylindrical, spherical, or Fresnel). It has implications on the meshing of the domain. Cylindrical and spherical LCALs are the easiest to mesh since their linear/circular electrodes have characteristic length scales on the same order as the rest of the domain. The exception to this is spherical LCALS with a thin ring electrodes, such as those in refs. [87, 70]. For example, ref. [87] has a hole patterned electrode with a diameter of 4 mm and a ring electrode with a width of 2 µm (0.002 mm), a 3 order of magnitude difference. Where spherical LCALs have sometimes used one ring electrode, Fresnel LCALs are made up of almost exclusively of ring electrodes, see Figure 3.4. This results in Fresnel lenses requiring the most complicated meshes, at least near the boundaries, of the three. For example, ref. [75] constructs a Fresnel LCAL with a diameter of 2.4 mm, but with ring electrodes as thin as 15 µm (0.015 mm) and spacing between adjacent rings of 3 µm (0.003 mm).

The next important consideration is the number of modelling domains. Multiple coupled LC domains are sometimes proposed in order to increase the optical power [88], achieve polarization independence [82], or decrease response time [89]. There is significant challenge in modelling multiple domains. As currently implemented, the model used in this thesis does not support multiple domains. Supporting multiple domains will require setting up the model so that only the relevant equations are solved in each domain, i.e. Gauss' law everywhere and the nematic orientation equation only in the LC layer.

3.3 LCAL Modelling Work in Literature

Modelling of a system is performed either to predict experimental results or to gain insight into them. Unfortunately, very little modelling has been and is being performed in the field of LCAL; most published research is almost entirely experimental. This is in contrast to the much more advanced field of conventional lenses, where initial design exploration and testing is done almost exclusively through software modelling. The models for liquid crystals, e.g. those discussed in section 2.4, are non-linear and involve multiphysics, thus far more computationally demanding than those for conventional lenses. This likely plays a significant role in the lack of modelling.

Some past research involved performing modelling using closed-source software either to gain insight into experimental results [90, 91] or to propose a new LCAL configuration and

predict its performance [92, 74, 93, 94, 95], though not all such works have experimentally validated their predictions. Unfortunately, being closed-source, the underlying models and numerical implementations are unavailable for verification and validation.

The papers which implemented their own model often used Frank-Oseen theory [96, 97, 98, 99, 100, 101, 102] rather than the more general and accurate Landau-de Gennes theory [56, 103]. Those that used Frank-Oseen theory share the shortcomings of that theory, see subsection 2.4.2. Additionally, further simplifications were often made to the model by neglecting at least the k_{24} term, though neglecting of further terms was often done [99]. Sometimes, even the one elastic term approximation, where all terms except k_{11} are neglected, was used [101]. A particularly interesting paper is ref. [96]. The authors use Frank-Oseen theory, but they rewrite it in terms of a simplified Q tensor, where uniaxiality is imposed, in order to address the issue of director headlessness. Research studies that used the Landau-de Gennes theory for LCAL modelling did not have the shortcomings of the Frank-Oseen versions, but have also not yet had their predictions experimentally verified.

Most of the modelling focused on single domain LCALs, despite experimental research into multiple domain LCALs being prevalent as early as the year 2000 [104]. One of the few exceptions is papers like ref. [74]; though they used a closed-source software package.

This topic will be investigated in greater detail in subsection 6.1.3 for the specific LCAL that will be modelled in this work.

3.4 Applications

LCALs have been designed to function similar to conventional lenses and, thus could replace essentially any conventional lens. However, given the relative infancy of the technology, the challenges of LCALs, and the need for a constant power source to operate, the applications currently being explored for LCAL are those which conventional lenses cannot achieve, or cannot achieve to a satisfactory level. Such applications are characterized by requiring a lens capable of focusing and/or zooming under severe space limitations. These applications range from medical to consumer electronics.

The first medical application is that of eye glasses [105, 106, 107] and contact lenses [108, 109]. For both of these applications, the goal is to use LCAL either on their own or in combination with conventional lenses to produce glasses/contact lenses whose prescription can be dynamically adjusted. The main benefit of this approach is for those who need bifocal or progressive glasses; rather than being limited to looking at objects in only certain

regions of their field of view, LCAL-based glasses would allow the wearer to once again look at objects in a more natural manner. An additional benefit is that it allows for glasses/contact lenses to be adjusted, rather than replaced, when the prescription changes.

Then there is the eye lens replacement procedure; LCALs are promising candidate for replacing the crystalline lens in the human eye, a common medical procedure for dealing with severe cataracts [110, 111, 112]. The advantages of a LCAL solution over other existing technologies are: a) LCALs can dynamically change their focus, and b) LCALS can change their focus without requiring muscle contractions. Point b) is a very significant advantage since eye musculature degrades with age.

The final medical application is in endoscopes, where LCAL has been used to create 2D-imagining endoscopes for previously infeasible applications [113] as well as 3D-imaging endoscopes [114].

The first consumer electronics use-case is for autofocus and zoom capabilities in cameras, particularly in smartphones where 2 and even 3 lenses are becoming standard [115]. This increase in lens count is a response to consumers wanting to "blur the background" and the ability to zoom in and out the way a dedicated camera can. Multiple lenses being the only solution to the problem is a direct result of the spatial limitations of the smartphone; a conventional zoom lens would simply not fit. A LC-based zoom lens is one possible solution, since it does not require any space to move while zooming [116]. In addition to zoom, a LCAL element can be used as the autofocus system for an otherwise conventional lens [117]. This approach can be faster and more reliable than conventional autofocus systems [101].

The next consumer application is in reducing eye strain in Augmented Reality (AR) and Virtual Reality (VR) applications. One of the major causes is "vergence-accommodation conflict" [118]. Focusing our eyes involves 2 actions: a) pointing both eyes at an object, b) adjusting each eye's lens to make the object clear. Each of these steps produces a distance measurement inside the brain, see Figure 3.6 for a visual representation.

When these two distances are not the same it induces eye strain. The problem for AR/VR applications is that vergence distance **must** be different then the physical distance of the screen from our eyes in order for us to perceive the images as 3D. The focal distance however is usually not changed, as that would required moving parts for which there is very little room. Research into using LCALs for this application has been done since LCALs could change that focal length without needing to move [120, 118] .

And finally, there are smart lighting applications. Current smart lights can be controlled through software to change their brightness and hue. However, the shape and direction of such lights is not currently controlled. LCALs have been proposed for such applications

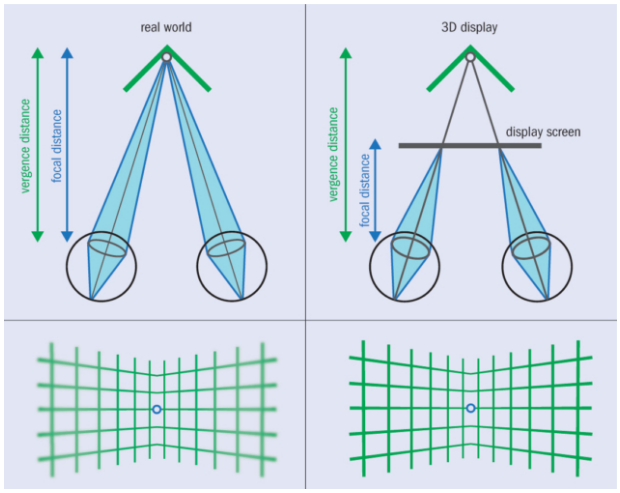

Figure 3.6: Vergence-accommodation conflict visualized. From [119].

to allow the beam shape, size, and position to be electronically controlled [121, 122], and such technology is being actively commercialized [123].

Chapter 4

Methods

This chapter will summarize the analytic and numerical methods used to solve the model laid out in chapter 2. First, the electric field model and the nematic free-energy models will be coupled. Then, the free-energy model for the nematic will be converted into an Euler-Lagrange form and subsequently into a transient PDE. Following this, an overview of the numerical methods used to solve the resulting coupled PDEs will be provided. Finally, a brief discussion of how the cross-polarization modelling.

4.1 Model Formulation

The model for the electric field and nematic texture were laid out in subsection 2.1.5 and section 2.4.3, respectively. The first step is to couple them together through the permittivity tensor. Having done that, we will have a partial differential equation and an equation for the total free-energy of the nematic phase. In order to minimize that free-energy, it will be converted from a functional to a partial differential equation through the calculus of variations. Subsequently, the resulting Euler-Lagrange equation will be converted into a transient problem by the addition of time-dependence into the model. This allows the model to converge to the correct equilibrium texture from a much broader range of initial conditions, as well as to capture the dynamics of the texture.

4.1.1 Coupling of Electric Field and Molecular Orientation

First, we make the simplification of assuming no dissipation within the material and relate the permittivity tensor to Q_{ij} as [124]:

$$\varepsilon_{ij} = \frac{\varepsilon_{\parallel} + 2\varepsilon_{\perp}}{3}\delta_{ij} + \left(\varepsilon_{\parallel} - \varepsilon_{\perp}\right) Q_{ij} \tag{4.1}$$

Then, we combine Equation 4.1 and Equation 2.18:

$$\partial_i \left(\frac{\varepsilon_{\parallel} + 2\varepsilon_{\perp}}{3}\delta_{ij} + \left(\varepsilon_{\parallel} - \varepsilon_{\perp}\right) Q_{ij} \right) \partial_j V = 0 \tag{4.2}$$

4.1.2 Free-Energy Minimization

The equilibrium texture is obtained by solving for the tensor field of Q_{ij} which minimizes the total free-energy of the system, Equation 2.41. The approach taken to minimize this functional is the application of the calculus of variation. It converts the function into the following Euler-Lagrange equations[1]:

$$\frac{\partial f}{\partial Q_{ij}} - \partial_k \frac{\partial f}{\partial \left(\partial_k Q_{ij}\right)} = 0 \tag{4.3}$$

with boundary condition:

$$\frac{\partial f_{surf}}{\partial Q_{ij}} + h_k \frac{\partial f}{\partial \left(\partial_k Q_{ij}\right)} = 0 \tag{4.4}$$

where h_k is the unit normal for the bounding surface.

One could attempt to solve Equation 4.3, and Equation 4.2, for Q_{ij} directly, but this would only converge if the initial guess was very close to the equilibrium solution. Instead, an initial condition can be evolved towards the equilibrium texture by introducing a time-dependence into the model:

$$\mu_r \frac{\partial Q_{ij}}{\partial t} = -\left[\frac{\partial f}{\partial Q_{ij}} - \partial_k \left(\frac{\partial f}{\partial \left(\partial_k Q_{ij}\right)} \right) \right]^{ST} \tag{4.5}$$

where μ_r is the rotation viscosity of the LC phase, and $[\cdot]^{ST}$ represents extracting the symmetric-traceless component of what's inside. The symmetric-traceless component must be extracted in order to keep Q_{ij} symmetric-traceless throughout the time evolution.

[1] Equations originated by Fred Fu [7].

Note that solving for the equilibrium Q_{ij} field requires knowledge of the electric potential field, V. But, solving for V requires knowledge of the alignment field Q_{ij}. Thus Equation 4.2 and Equation 4.5 are coupled, and must be solved simultaneously in order to arrive at the correct equilibrium solution.

4.2 Numerical Methods

4.2.1 Finite Element Implementation

Equation 4.2 and Equation 4.5 represent a system of coupled transient non-linear PDEs. These equations will be solved numerically in Python using the open-source finite element method package FEniCS [125]. The finite element method was chosen since it can handle the unstructured grid that will be required to capture the complicated geometry of some LCALs, such as Fresnel LCALs. The work in this thesis will use 1st order (linear) Lagrange polynomial basis functions. Additionally, since this work will be specifically focusing on a simple LCAL geometry as a starting point, a structured and uniform grid will be used. The mesh used in this work will be manually generated using the functionality provided by FEniCS. In order to use the finite element method, the coupled PDEs must first be converted into their weak forms. This is done by multiplying the equations by a weighing function and integrating over the domains. Equation 4.5 is combined with Equation 2.41, and the weak form is[2]:

[2]The Landau-de Gennes portion of the weak form was originally developed by Fred Fu [7], and the spatially varying electric field portion by Jake Ferguson [8]

$$
\begin{aligned}
0 = & \iiint_\Omega \left[\mu_r \frac{\partial Q_{ij}}{\partial t} v_{ji} \right] \, \mathrm{d}\Omega \\
& + \iiint_\Omega \Bigg[\left(aQ_{ij} - b(Q_{ik}Q_{kj} - \frac{1}{3}Q_{kl}Q_{lk}\delta_{ij}) + c(Q_{kl}Q_{lk}Q_{ij}) \right) v_{ji} \\
& \quad - \left(\frac{\varepsilon_0}{2}(\Delta\varepsilon)(\partial_i V \partial_j V - \frac{1}{3}\partial_k V \partial_k V \delta_{ij}) \right) v_{ji} \\
& \quad + L_1(\partial_k Q_{ij}\partial_k v_{ji}) + (L_2 + L_{24})\left(\frac{1}{2}(\partial_i Q_{kj}\partial_k v_{ji} + \partial j Q_{ki}\partial_k v_{ji}) - \frac{1}{3}\partial_l Q_{lk}\partial_k v_{ji}\delta_{ij} \right) \\
& \quad + L_3 \left(Q_{kl}\partial_l Q_{ij}\partial_k v_{ji} + \frac{1}{2}\partial_i Q_{kl}\partial_j Q_{kl} v_{ji} - \frac{1}{6}\partial_k Q_{lm}\partial_k Q_{lm}\delta_{ij} v_{ji} \right) \\
& \quad + \left(\frac{\varepsilon_\parallel + 2\varepsilon_\perp}{3}\delta_{ij} + (\Delta\varepsilon)Q_{ij} \right) \partial_j V \partial_i v_{ji} \Bigg] \, \mathrm{d}\Omega \\
& + \iint_\Gamma \left[\alpha \left(Q_{ij} - Q^s_{ij} \right) v_{ji} \right] \, \mathrm{d}\Gamma
\end{aligned}
\tag{4.6}
$$

The weak form of the electric potential is[3]:

$$
\begin{aligned}
0 = & \oint_\Gamma n_i \left(\frac{\varepsilon_\parallel + 2\varepsilon_\perp}{3}\delta_{ij} + \left(\varepsilon_\parallel - \varepsilon_\perp \right) Q_{ij} \right) \partial_j V \nu \, \mathrm{d}\Gamma \\
& - \int_\Omega \left(\frac{\varepsilon_\parallel + 2\varepsilon_\perp}{3}\delta_{ij} + \left(\varepsilon_\parallel - \varepsilon_\perp \right) Q_{ij} \right) \partial_j V \partial_i \nu \, \mathrm{d}\Omega
\end{aligned}
\tag{4.7}
$$

4.2.2 Time Stepping

In addition to being discretized in space, Equation 4.6 must also be discretized in time. This was done using the method of lines [7]. Given the wide range of timescales found during this process, an adaptive time stepping method was used in order to speed up computation. At each time step, $Q_{ij}^{(t+\Delta t)}$ and $V^{(t+\Delta t)}$ are computed twice; first with a single time step, Δt, and a second time using two consecutive steps, each of size $\frac{\Delta t}{2}$. These two results are used to estimate the local error, which is then used to either increase or decrease Δt [7].

[3]The weak form of Gauss' law used here was originally developed by Jake Ferguson [8]

4.2.3 Periodic Domain

Both the LCD and LCAL cells to be modelled are constructed out of a repeating unit which is tiled in the x and y directions. Thus, to save computation resources, we will be taking advantage of this periodicity to significantly reduce the computational domain.

4.2.4 Boundary and Initial Conditions

The two equations set up above will require boundary and initial conditions for both molecular orientation and electric potential. Each of these conditions were handled differently.

For the LC orientation, the surface anchoring was handled through the free-energy term, rather than a Dirichlet boundary condition, as described in section 2.4.3. For the initial condition, there exist three options for an initial condition: isotropic, random orientation at every point, and a user specified condition. The first two conditions would require significantly more time to obtain the equilibrium texture when compared against a well chosen specific initial condition. Thus, in order to speed up the computation, the initial condition for the molecular orientation was chosen so that it would satisfy the surface anchoring in the absence of an electric field, or at least be chose to a texture that would. E.g. for a rectangular cell with homeotropic anchoring at the top and bottom surfaces, the initial condition used would be a vertical alignment everywhere in the cell. The exact condition specified is problem dependant and will be discussed in chapter 5 and chapter 6.

For the electric potential, the boundary condition for each electrode is handled as a Dirichlet boundary condition, fixing the electric potential as that of the electrode. As with the orientation, a good guess for an initial condition can result in significant speedups. The initial condition was found by solving only Gauss' law and taking the spatial distribution of ε_{ij} as fixed. The result was then used as the initial condition for the full model. This was done in order to speed up the computations, as without this step the model takes about 3–5 times longer to solve.

4.3 Cross-Polarization Microscopy

Once the equilibrium texture has been obtained, the next step is to compare against experimental observable results, i.e. those that would be obtained from cross-polarization microscopy as discussed in subsection 2.2.3. To do this, the cross-polarization microscopy results corresponding to the equilibrium textured are modelled using the open-source Python

package “dtmm” [126]. This package models the propagation of electromagnetic waves by solving Maxwell’s equations. Models for doing thisinclude the Jones matrix method [13] and Berreman’s matrix method [127]. Both of these methods solve Maxwell’s equations by discretization the domain into layers perpendicular to the direction of propagation. Berreman’s method is more comprehensive and general than the Jones method; especially the regular 2x2 Jones matrix version which does not handle reflections and oblique incoming rays. As such, the full Berreman 4x4 method was chosen and used.

Note that the molecular orientation is assumed fixed in space and unaffected by visible light for the purpose of modelling cross-polarization microscopy. Given the low light intensities, and subsequently low electromagnetic field strengths, this is a reasonable assumption.

Chapter 5

Modelling of LCD Cells

In order to validate the model, two common LCD cells, the TN and IPS cells, will be modelled. The TN cell was chosen for its simplicity, and the IPS cell for the similarity of its geometry with that of the LCAL to be tested in chapter 6. Both of these cells will be modelled using a nematic material whose model and physical parameters are readily available in literature. Finally, the equilibrium texture and cross-polarization results will be compared against expected results.

5.1 Background

5.1.1 TN Cell

A visualization of the TN cell is shown in Figure 5.1. It features a LC layer with a glass substrate above and below it. The side of the glass substrates facing the LC is coated with a flat transparent electrode. A thin polyamide layer is coated onto these electrodes and then physically rubbed so that the LC aligns itself parallel to the glass and along the direction of rubbing. The direction of this rubbing on the top and bottom layers are perpendicular to one another. Finally, on the other side of each glass layer is a linear polarizing filter, whose direction polarization direction is parallel with the rubbing direction on the end of the cell.

When no electric potential difference is applied between the electrodes, the LC will align itself to the surface at either end of the cell and twist smoothly, hence the name, between these two perpendicular orientations. This is shown in Figure 5.1. This twist

rotates the polarization of the entering light 90°, allowing it to pass through the second polarizing filter, showing up as bright cell. When an electric potential difference is applied between the electrodes, an electric field is formed through the cell with field lines pointed perpendicular to the two rubbed surfaces. This field causes the LC molecules to align themselves perpendicular, for the most part, to the surface. In this orientation, the LC will not influence the polarization of the light. The light will therefore not pass through the second polarizer, resulting in a dark pixel.

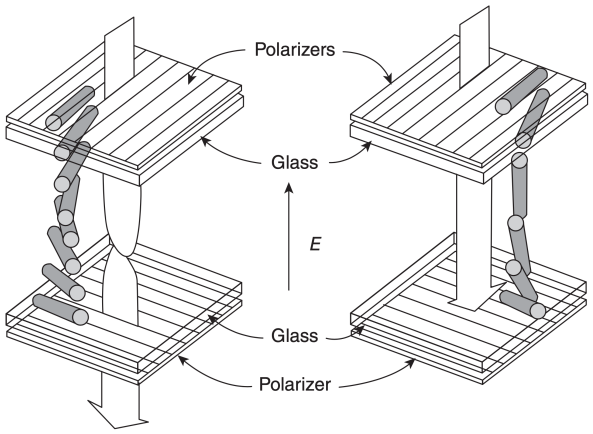

Figure 5.1: Texture of a TN cell in the light state (left) and dark state (right). From [128].

5.1.2 IPS Cell

Like the TN cell, the IPS cell acts like a light shutter. The difference is that instead of changing its texture by rotating vertically, it will rotate in the plane. This is achieved through a more complex electrode structure. The LC has the same polyamide layers and rubbing as the TN cell, resulting in a twisted texture in the absence of an applied field. The important difference is that the both electrodes are on the same side of the cell. They are set up in an interdigitating pattern of alternating positive and negative electrodes, as shown in Figure 5.2. Again, we will be taking advantage of periodic boundary conditions, in order to limit the modelling domain to a single repeat unit, shown in the pink rectangle in Figure 5.2. This repeat unit consists of one positive electrode, red in the figure, and one negative electrode, blue in the figure, and together forms two pixels.

Further, unlike a TN cell which has its analyzer and polarizer crossed, an IPS cell has the axes of its analyzer and polarizer parallel. Thus, when the electrodes are turned off,

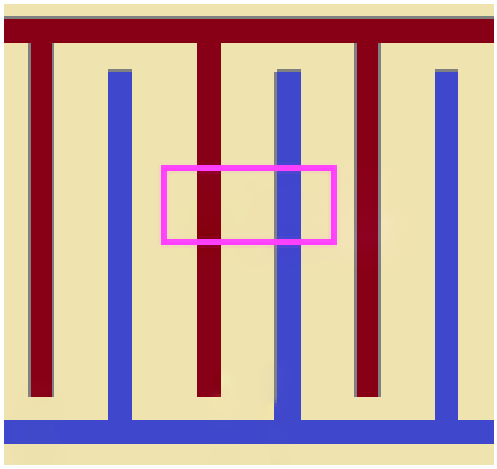

Figure 5.2: The interdigitating electrode structure. From [129].

the twisted texture results in a dark state. When the electrodes are turned on, an electric field is formed between them, with field lines that run, mostly, horizontal and parallel to the rubbing direction of the opposite surface. This is not true of everywhere in the cell; especially above the electrodes, slightly to either side of them, and on the surface. The molecules will reorient themselves to line up with the field, thereby undoing the twist; this results in a overall bright state since the the polarization of light is no longer being rotated. This behaviour is shown in Figure 5.3, where the electrodes are labelled as "e1" and "e2". Note that this diagram does not show the entirety of the texture, specifically it does not show what happens to the molecules on the bottom surface, and it does not show what happens above the electrodes.

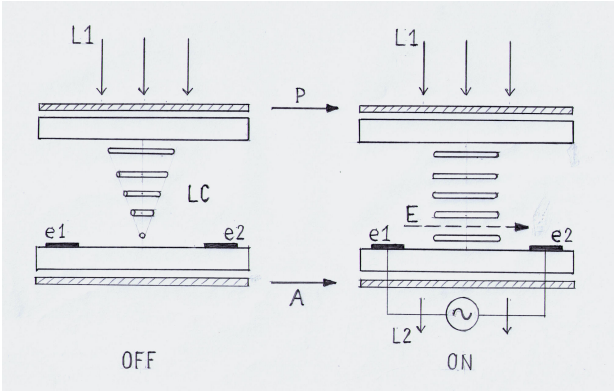

Figure 5.3: An IPS cell in its dark and light states, left and right respectively. From [130].

5.2 Methodology

The TN and IPS cells will be modelled under two conditions: electrodes turned off and turned on. The first modelling run will obtain the equilibrium texture associated with the electrodes turned off. The initial condition for both the TN and the IPS cell will be halfway between the two boundary conditions; one surface is anchored in the x-direction and the other in the y-direction, therefore initial condition will be at a 45° between the two. The second modelling run will find the equilibrium texture with the electrodes turned on. The initial condition used for this modelling run is the equilibrium condition from the electrodes turned off.

The equilibrium textures of each of these runs will be displayed using director glyphs, shown as rectangular prisms whose long axis points along the director. Then, polarized microscopy modelling will be performed on each of the equilibrium textures.

The nematic material used for the modelling is 5CB; its material's properties are listed in Table A.1. The cell specific parameters for each for the TN and IPS cells are show in Table 5.1 and Table 5.2, respectively.

Table 5.1: TN cell parameters

Parameter	Value	Unit
Element size	0.2	µm
Cell size in x	2	µm
Cell size in y	2	µm
Cell size in z	10	µm
Electrode potential	10	V

Table 5.2: IPS cell parameters

Parameter	Value	Unit
Element size	0.2	µm
Cell size in x	10	µm
Cell size in y	2	µm
Cell size in z	2	µm
Electrode width	1.5	µm
Electrode spacing	3.5	µm
Electrode potential	10	V

5.3 Results

5.3.1 TN Cell

We will start with the equilibrium texture for the TN cell. The expected texture was described in the subsection 5.1.1, and looking at the modelling results in Figure 5.4, we can see that the expected texture is obtained. Figure 5.4(a) shows the smooth twist texture between the rubbing directions of the top and bottom layer that occurs in the absence of an electric field.

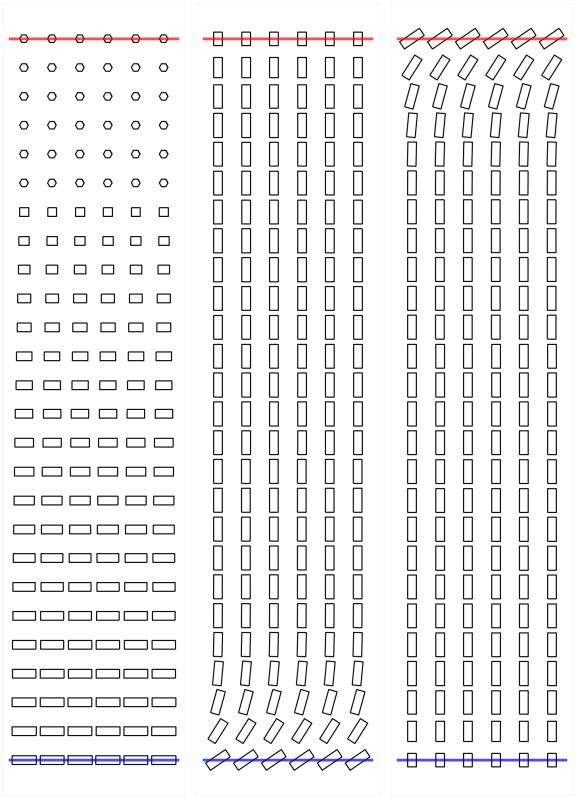

(a) (b) (c)

Figure 5.4: Equilibrium texture model results of the TN cell with the: (a) electrodes off, (b) electrodes on and view parallel to bottom anchoring direction, (b) electrodes on and view parallel to top anchoring direction.

Further, when the electrodes are turned on, this twist texture is replaced by a mostly vertical texture. This is shown in Figure 5.4(b) and (c) from two different angles, first with a view parallel to the bottom surface anchoring and the second view parallel to the top surface anchoring. The texture is mainly vertical in the bulk of the cell where the electric free-energy contribution dominates. However, the texture has a significant horizontal component as one approaches the surface due to the increasing competition between the electric and surface free-energies. If the electric potential was further increased, the resulting texture would be increasingly vertical as the electric free-energy would become ever larger than the surface free-energy.

With the equilibrium texture matching literature,we move on to the cross-polarization microscopy results. The analyzer and polarizer are aligned parallel to the rubbing directions at their corresponding surfaces. As mentioned previously, a bright cell is expected when the electrodes are turned off, and a dark cell then they are turned on. As can be seen in Figure 5.5, the expected results are obtained.

(a) (b)

Figure 5.5: Cross-polarization result of TN cell, (a) Electrodes turned off, (b) Electrodes turned on.

5.3.2 IPS Cell

Having successfully reproduced the correct equilibrium texture and cross-polarization microscopy results for the TN cell, the IPS cell will be investigated. The equilibrium texture for the IPS cell is shown in Figure 5.6. Again, the electrodes have been overlayed, red for positive and blue for negative. Beginning with the case of the electrodes turned off, the correct texture is observed in Figure 5.6(a): a smooth 90° twist, aligned in the plane

at the top surface and out of the plane at the bottom. When looked at from below in Figure 5.6(b), it can be seen that the orientation is not perfectly vertical, i.e. in line with the rubbing direction. This is due by the competition between the surface anchoring and elastic free energies.

Next, the electrodes are turned on. The equilibrium texture is again shown from two angles in Figure 5.6: (c) from the side, and (d) from below showing *only* the alignment on bottom surface. Note, in order to make the analysis of the results easier, only one of the two pixels in the repeat unit are being shown; the results have been cropped to the area between the electrodes and include half of each electrode.

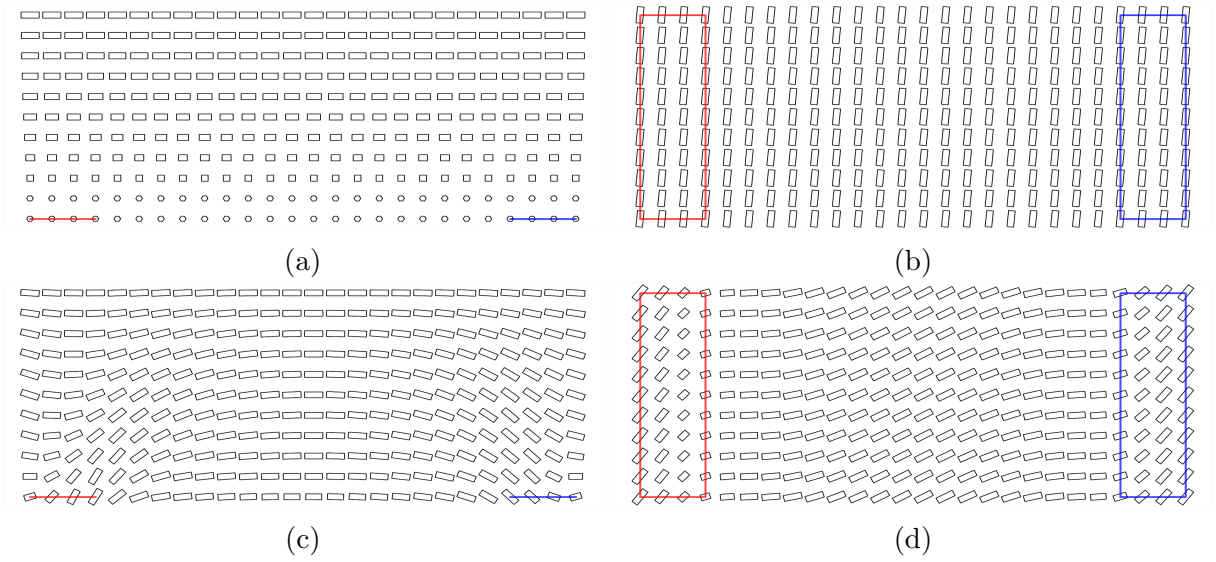

Figure 5.6: Texture of IPS cell. Electrodes off: (a) side view, (b) bottom view of bottom surface. Electrodes on: (c) side view, (d) bottom view of bottom surface.

When looking at the texture in Figure 5.6(c) that the resulting texture is more complex than having all molecules orientated horizontally in the plane of the image. The domain will be broken up into two parts for discussion: 1) the centre region in-between the electrodes, and 2) above and to the side of the electrodes.

First is the region between the electrodes but above the surface, directly in the middle of each of the subfigures. In this region we see that the twisted texture has been undone, with the molecules reorienting themselves to be parallel to the anchoring at the top surface. However, looking at Figure 5.6(d) we see that the molecules on the bottom surface have not completely reoriented. This is because of the competition between the surface anchoring

and the electric forces. Both the surface anchoring and the electric torque have a preferred orientation that would minimize their respective free-energy. The surface free-energy would be minimized by having the molecules in (d) pointing vertically, while the electric free-energy would be minimized by having the molecules pointing horizontally. Unfortunately, these two orientations are orthogonal to each other, and thus the equilibrium orientation will be based on the relative strength of each force. Given that the bottom equilibrium orientation is not perfectly horizontal, it is expected that a slight twist in the texture will remain in this region. This slight twist is expected influence the polarization of light, and result in a slightly darker region in the middle under cross-polarizers.

Next is the region above and just to the side of the electrodes. From Figure 5.6(c), it can be seen that the alignment in this region is not horizontal. The reason for this alignment is the same as for that occurring between the electrodes, the torque exerted by the electric field. The molecules reorient to align themselves along the electric field lines, unfortunately these field lines are not horizontal in this region. Looking at the same region from below, Figure 5.6(d), it can be seen that molecules along the bottom surface in this region also are not aligned parallel to the anchoring on the top surface. This again is due to the competition between the surface anchoring and the electric field free-energy. With the electrodes turned off, the equilibrium texture has the molecules at the surface oriented parallel to the surface. And, when the electrodes are turned on, the electric field lines that come out from the top of the electrodes are mostly in the vertical direction, i.e. mostly perpendicular to the molecules. Thus the electric field exerts little torque on these molecules and therefore does not reorient to a large degree. The texture in this area is more aligned to the surface anchoring than that twisted area in the middle of the electrodes, but it is also much narrower. Thus we would expect to see a dark region here, but one that is darker and narrower than that found in-between the electrodes.

Note that a large part of the discussion has been about the competition between the surface and electric free-energy contributions. Had Dirichlet boundary conditions been used, there would be no reorientation of the molecules at the surface.

Having investigated the equilibrium texture and found the results good, the polarization microscopy modelling is performed on the textures. Based on the discussion above and on the literature, it is expected that the polarization microscopy results will feature a uniformly dark cell when the electrodes are off and a unevenly lit bright cell when they are on. That is in fact what the polarization microscopy results Figure 5.7 shown. Note, the results in this figure, as in Figure 5.6 have also been cropped. Further, the contrast of Figure 5.7(b) has been increased in order to show the non-uniform illumination

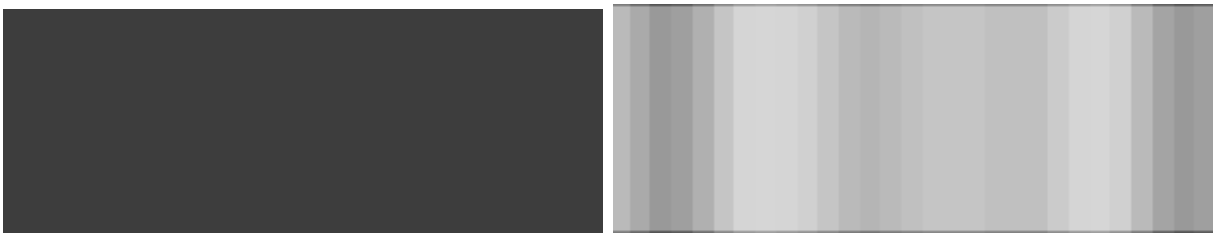

(a) (b)

Figure 5.7: Cross-polarization result of IPS cell, (a) Electrodes turned off, (b) Electrodes turned on.

5.4 Summary

The resulting TN texture matches up with expected results; a twisted texture when the electrodes are turned off, and an untwisted and mostly vertical texture when the electrodes are turned on. The corresponding cross-polarization microscopy results also match up with expectations; a bright state when the electrodes are off, due to the rotation of the light's polarization, and a dark state when they are on, due a lack of rotation.

Moving on to the IPS cell, there too the expected results are obtained. With the electrodes turned off, the correct twisted texture is seen. Further, the cross-polarization results show a uniformly dark cell.

When looking at the texture for the electrodes turned on, the results appear correct and are understandable. The discussion of this texture was conducted in two parts.

First, the region between the electrodes. Away from the bottom surface, the molecules had reoriented to point almost entirely along the field lines. Near the surface, the molecules were not fully aligned with the field lines because of the competition between the surface and the electric free-energies.

Next, the region above and directly beside the electrodes. The molecules here are have not reoriented to be horizontal and parallel to the anchoring on the top surface since that is not the form of the electric field lines in this region. The field lines here have a significant vertical component, hence the significant vertical component in the alignment of the molecules. The molecules on the surface in this region have only slightly reoriented in response to the electric field. This is because the molecules there are parallel to the electrode's surface when the electrode is turned on. The field lines at that surface are mostly vertical, and hence perpendicular to the molecules. This results in a twisted texture above part of the electrode, a region which shows up as slightly darker when polarization

microscopy modelling is performed. This non-uniform texture was expected to produce a bright cell with non-uniform illumination; darker regions were expected where a slight twist remained. This non-uniform illumination in the bright state of the cell were observed.

Having shown that the model is capable of producing the expected texture and cross-polarization results for both the TN and IPS cell, it is time to now move on to the more complicated task of modelling a LCAL.

Chapter 6

Modelling of a LCAL

Having shown that the model reproduces the expected results for the TN and IPS cells, we will now model a single domain voltage controlled LCAL. First, a discussion of the criteria by which a LCAL was chosen out of the many designs in the literature. Then, a brief overview of the LCAL chosen. Following this is a discussion of past modelling of this LCAL. Finally, the texture and cross-polarization modelling results are compared to results in literature, both experimental and modelling.

6.1 Background

6.1.1 Criteria for Choosing a LCAL

In the previous chapter, two LCD technologies were chosen, the TN and IPS cell, based on their successful commercialization and importance to the field. Unfortunately, given the infancy of the LCAL field, no such equivalent designs are available. Instead, the LCAL design to model will be chosen based on three criteria.

First is the availability of published results. Experimental cross-polarization microscopy results are readily available. However, as discussed in chapter 3, very few LCALs papers feature any modelling. Without modelling results, it will be much more difficult to ensure that we obtain the correct texture. We will therefore limit ourselves to those LCAL design which have both modelling and experimental results.

Next are the modelling requirements. As discussed previously, the model currently only supports voltage control and single domain LCALs. Thus a simple design is required.

And finally, there is the ease of production. As mentioned, linear electrodes are easier to manufacture than hole-patterned, ring, or Fresnel electrodes since they are simpler and can leverage existing LCD manufacturing expertise.

Based on these three criteria, the design from ref. [67], referred to as an HMD cell, is chosen. It fit the above criteria very well. First, there exist published results about this design, both from experimentation and from modelling. Next, it is easy to model since it features a single LC domain, easy to mesh electrodes, and voltage control. Finally, the design is easy to manufacture since it uses linear electrodes.

An in-depth exploration of the design, and past modelling work done on it are the subject of the following two subsections.

6.1.2 The HMD Cell

It was first proposed as a cell for LCDs, and referred to as the Homeotropic to Multidomainlike (HMD) cell [131]. The design was subsequently patented in 2000 for display applications [132]. A decade later a new patent was filed for using the cell in lensing applications [67], specifically for beam broadening (e.g. spotlights). Subsequently the cell was also investigated for use in producing privacy windows [133].

We will begin the discussion of the HMD cell's function as a LCAL with its geometry, shown in Figure 6.1.

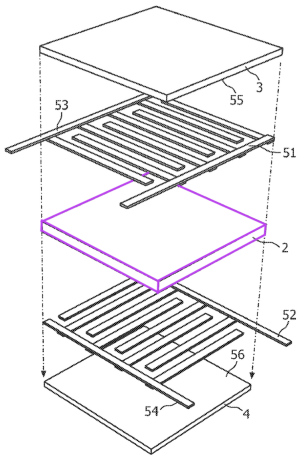

Figure 6.1: Exploded diagram of the HMD cell, showing the LC layer and the orientation of the interdigitating electrodes. From [67].

The cell is comprised of a LC layer, labelled as 2 in the figure, with glass substrates above and below it, 3 and 4. The surfaces of the glass substrates facing the LC layer have the electrodes printed onto them, 51–54. The electrodes on each surface use the same interdigitating linear electrode structure as an IPS cell. The electrodes on above the LC are arranged to be perpendicular to those below the LC. Over these electrodes, directly in contact with the LC layer, is deposited a thin alignment layer, not pictured, which promotes the homeotropic alignment of the molecules.

As with the IPS cell, the HMD cell features a repeating unit in the x-y directions. To facility the discussion, and later the modelling, we shall limit ourselves to a single repeat unit. This repeat unit is shown in Figure 6.2, as would be seen when looking down the z-axis.

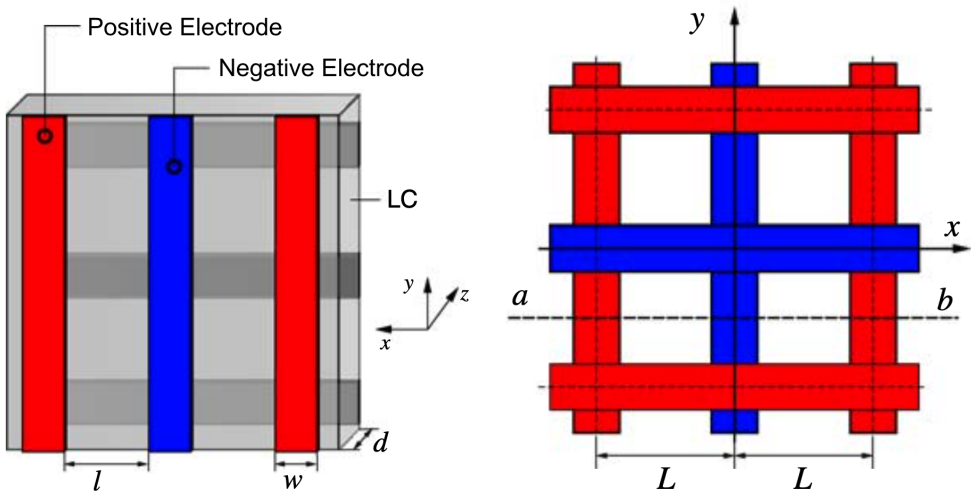

Figure 6.2: Top-down view of the HMD cell: (a) electrodes and cell parameters labelled, (b) view showing the overlap of the electrodes on either side of the LC layer. From [134].

Having gone over the physical construction of the HMD cell, it is time to describe its function. The HMD cell falls into the category of "lenses" described in chapter 3 that construct a spherical LCAL by stacking two perpendicular cylindrical ones. While other designs would have each cylindrical lens in its own LC layer, this design has them both being formed within a single LC layer. The functioning of one of these cylindrical lenses, when the electrodes are turned on, is depicted in Figure 6.3.

It must be noted that the HMD cell does not technically qualify as a lens since, among

other things, it does not have a singular focal point. The region between a pair of electrodes function as a cylindrical lens and has a focal line, but the device as a whole does not function as a lens since it has multiple focal points, one for each square aperture. However, this device will still be referred to as a LCAL for the sake of readability.

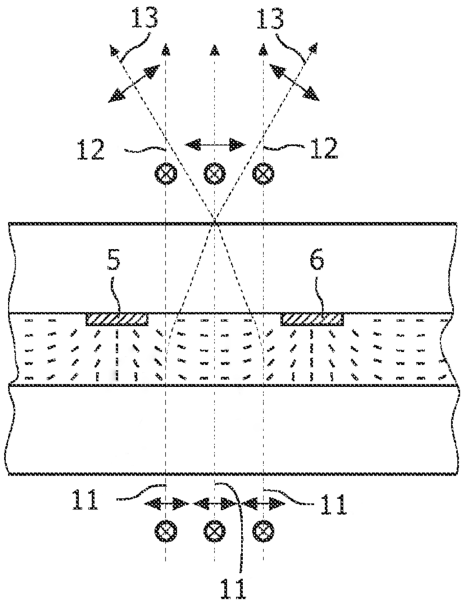

Figure 6.3: Side view layer with single cylindrical lens showing the texture and how it would expand light. From [67].

The unpolarized incoming light, 11 in the figure, is mathematically decomposed into two perpendicular linear polarization, one in the plane of the page and one out of the plane. When the incoming unpolarized light enters the lens, the component of light whose polarization is parallel to the plane will be broadened in the plane, labelled as 13. Further, the other linear polarization of light, the one oscillating out of the plane, passes through unaffected. Notice that as a cylindrical lens, it broadened light in only one direction; another cylindrical lens, acting on the same polarization but broadening it in the other direction, is required to uniformly broaden the light. For the time being however, we will limit our modelling to only a single HMD cell; the model does not currently support multiple LC domains, and published cross-polarization results for stacked HMD cells are not available.

Having discussed how the HMD cell is supposed to function as a lens, it is time to discuss the previous modelling work that has been done on it.

6.1.3 Previous Modelling Work

As mentioned in chapter 3, most LCAL research does not involved modelling; the HMD cell was chosen for being one of the few designs that have been modelled [135, 133].

The first group to model the HMD cell did so using Frank-Oseen theory [135]. As described in subsection 2.4.2, this theory is limited by its assumptions of uniaxiality and of a constant degree of alignment, S, as well as its inability to resolve defects. Additionally, Dirichlet boundary conditions are used for the homeotropic anchoring, rather than a free-energy contributions. Furthermore, this paper and its followups, refs. [136, 96], focused on producing approximate solution to this model in order to improve the computation. While they were successful, citing a speedup of 60-80x [96], they did by using significant simplifications to the general model. Including:

- Based on the experimental cross-polarization results, the authors argue for the further shrinking of the modelling domain. Instead of the repeat unit shown in Figure 6.2, the authors simplify it to a triangular prism with $1/8^{\text{th}}$ the volume [96]. This may seem similar to the use of periodic boundary conditions, but it is in fact profoundly different. The periodic boundary conditions are a numerical technique used to solve a general model; the symmetry simplifications implemented in ref. [96] are incorporated into the model itself, making it far less general.

- The domain is broken up the z-direction into three layers based on the distance from the electrodes [135]. Each of these layers is subsequently treated with different simplifications; e.g. near the electrode the twist elastic energy term is neglected, but in the bulk the *entire* elastic free-energy is neglected.

The problem with this approach is that is relies heavily on *prior* knowledge of the resulting texture. This would be adequate for examining the texture of experimental results for a specific cell geometry, but it is not a general model. It is not capable of predicting the resulting texture of a previously untested LCAL; this being the end goal of the model being developed in this thesis.

The second group to model the HMD cell did so using a close-source software package [133]. Unfortunately, they do not specify which model they used, or even if it was a vector or tensor representation, and they do not specify how they represented the surface anchoring. Their resulting texture looks qualitatively similar to that from ref. [135], but a direct comparison is not possible since it was visualized in a different manner.

Neither of the two groups discussed so far performed any cross-polarization microscopy modelling of their textures. Thankfully, the model presented in ref. [135] was subsequently

used by another group to produce cross-polarization microscopy results [134]. The cross-polarization results from this paper and from experiments will be compared against the results from the model in this thesis.

6.2 Methodology

As described above, this LCAL design has been modelled by two different groups, once using E7 and again using an unspecified LC material. Since not enough material parameters could be obtained for either material, the LCAL was instead modelled using 5CB. The properties used are the same as for the two LCD cells, and can be found in Table A.1. The geometric parameters of the cell are listed in Table 6.1.

Table 6.1: Physical cell parameters

Parameter	Value	Unit
Electrode potential	14	V
w	10	µm
l	20	µm
d	10	µm
Domain size in x	60	µm
Domain size in y	60	µm
Domain size in z	10	µm
Element size in x and y	0.4	µm
Element size in z	0.2	µm

Beyond the physical domain sizes, there are also boundary and initial conditions to specify. The HMD cell has homeotropic anchoring at the top and bottom surface, these were implemented with a surface free-energy term. The initial condition used was vertical orientation of the molecules throughout the domain; it is the equilibrium texture for the cell in the absence of an applied electric field.

As with the IPS cell, the HMD cell features a repeating pattern in the x-y plane. The repeat unit being modelled is shown in Figure 6.2. The origin is defined at the very centre of this repeat unit on the bottom surface, seen in Figure 6.2(b), and extends out a distance of L in both x and y. The ends of the domain at $x = \pm L$ are set equal to each other, the same with $y = \pm L$.

6.3 Results

As before, the discussion begins with the equilibrium texture. Figure 6.4 and Figure 6.5 provide comparisons between the equilibrium texture from this model and that from ref. [135]. The texture results in these figures are taken from the top-right square aperture that can be seen in Figure 6.2(b).

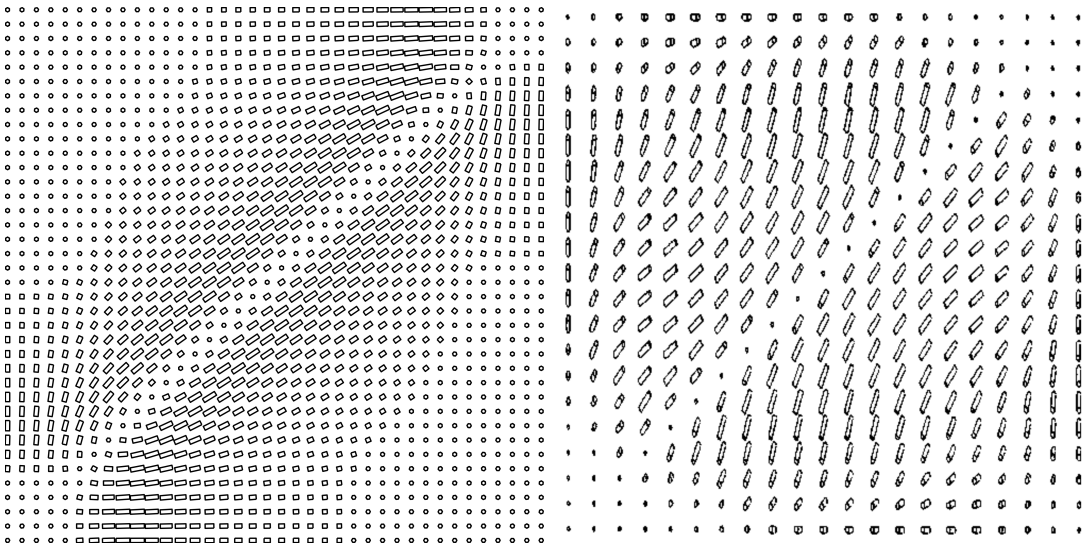

(a) (b)

Figure 6.4: Comparison of the equilibrium texture along the x-y plane at $z = 0.6d$: (a) this work, (b) from [135].

The resulting textures can be seen to *not* be in good agreement. We will begin with a discussion of the similarities. Both the texture from this work and that from literature feature a diagonal, bottom-left to top-right in Figure 6.4, where the molecules remain oriented essentially vertically. Furthermore by looking at Figure 6.5, we can see that this vertical alignment along the diagonal of the cell extends through the entire thickness of the cell. The molecules in this region stay close to their preferred anchoring direction for the same reason those above the electrodes in the IPS cell did, they are perpendicular to the electric field lines. Given this texture, it is expected that the diagonal will show up as a black line under cross-polarization microscopy since the vertical orientation will not affect the polarization of incoming light.

Now, let us discuss the differences. Starting with Figure 6.4, we can see that the published results feature reorientation essentially all along the edges of the square aperture,

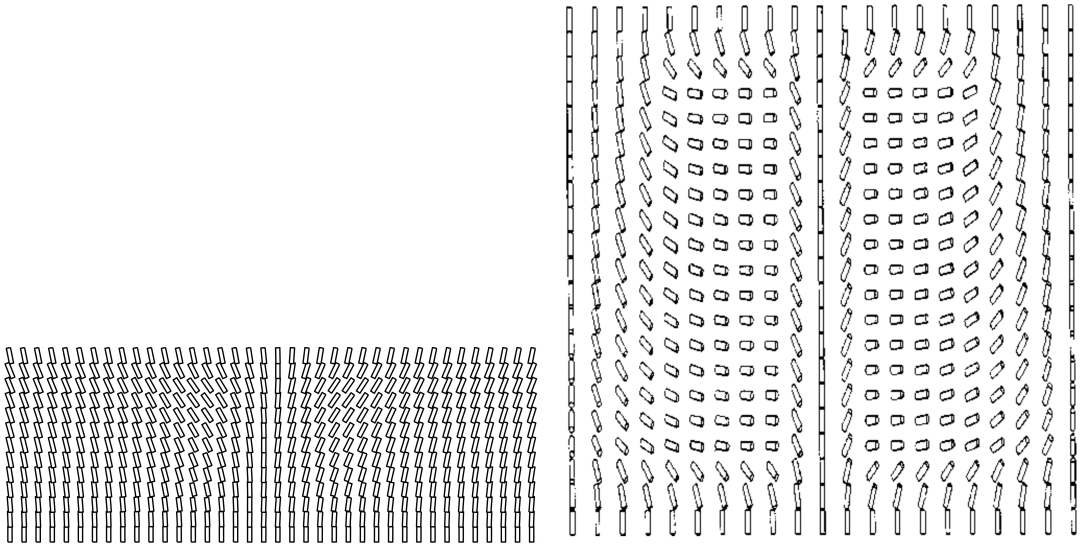

(a) (b)

Figure 6.5: Comparison of the equilibrium texture along the y-z plane in the centre of the square aperture. (a) this work, (b) from [135].

except for the very corners. The results from this work do not feature this reorientation. Further, while both results feature a reorientation of the molecules to a mostly horizontal orientation on either side of the diagonal, the texture from literature has this reorientation over a much larger area.

Moving on to Figure 6.5, it can be seen that the texture again varies considerably. The published results features two rectangular regions on either side of the centre in which the orientation is mostly horizontal and twisting out of the plane. The results of this work do not show that same texture.

Given that the textures were not in agreement, it is expected that the cross-polarization results won't be either. They are shown in Figure 6.6. These results are split into two rows based on the rotation of the analyzer and polarizer. In the top row, (a)–(c), the analyzer and polarizer are oriented horizontally and vertically, while in the bottom row, (d)&(e), they are oriented along the diagonals.

Looking at the top row, the experimental result, (a), shows dark regions above the electrodes and along the diagonals of the cell as well as 8 triangular bright regions. Next are the results from this work, (b), which look only mildly similar to the experimental results. There are dark regions above the electrodes, though not entirely, and there are the

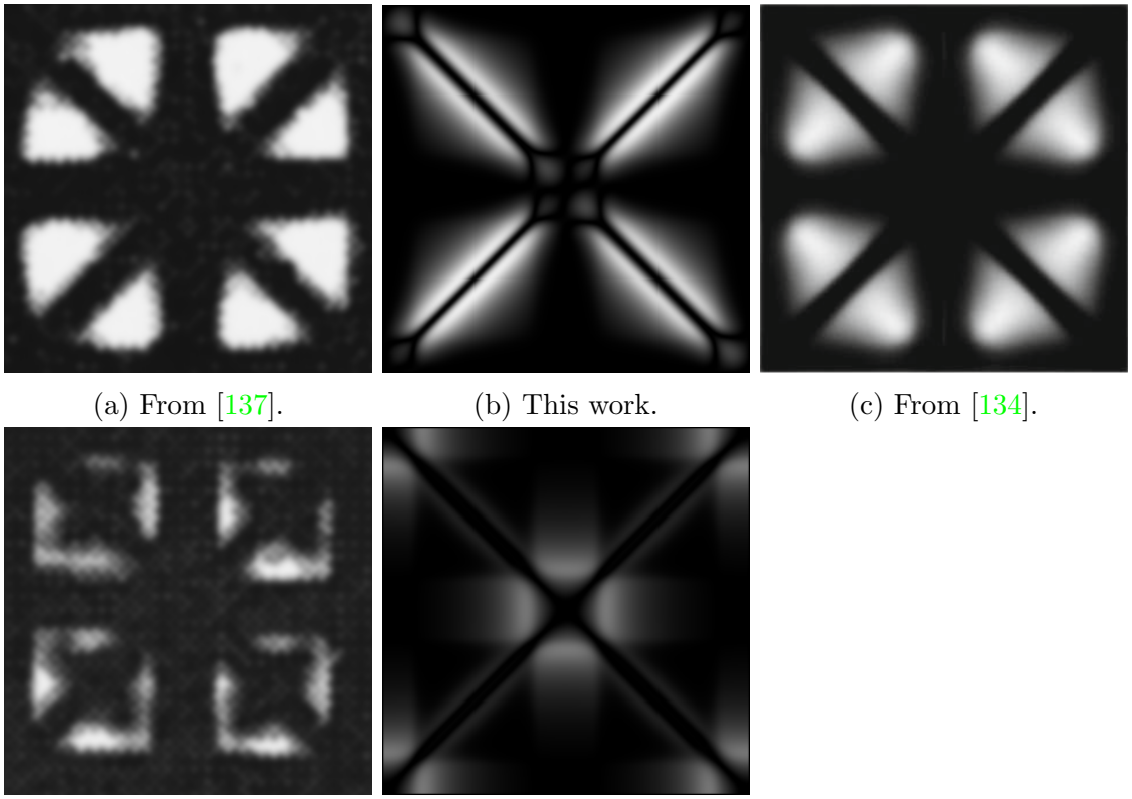

(a) From [137]. (b) This work. (c) From [134].

(d) From [137]. (e) This work.

Figure 6.6: Cross-polarization results. Top row: polarizer and analyzer running horizontally and vertically with respect to the page. Bottom row: polarizer and analyzer at -45° and 45° with respect to horizontal.

black diagonal regions, though much thinner. The triangular bright regions do not have the correct shape. Further, there are extra bright regions where the electrodes from the top surface overlap with those from the bottom surface.

Finally, there is the published modelling result, (c). It appears, qualitatively, to be in very good agreement with the experimental results. It show a less uniform illumination of the bright regions, something that the published experimental result do not. Through this can be easily due to the poor image quality of the experimental results.

Moving on the second row, the results agree even less. The experimental results, (d), features the same dark regions seen previously, but the bright regions have changed shape. Where they used to be triangular, they now have more complicated and harder to describe

shape. As for the result from this work, (e), the only similarity between it and the experimental result is the presence of the dark diagonal lines, but, as before, they are much thinner than the experimental ones. Unfortunately, ref. [134] did not provide any which were comparable with (d), nor did any other source.

6.4 Investigation the Discrepancy in Results

Given that neither the equilibrium texture nor the cross-polarization results were obtained, an investigation into the cause of the discrepancies was performed. It began with with the LC model, as until the textures are the same, it will be assumed the cause of all discrepancies in the cross-polarization microscopy results. Unfortunately, given the non-linear nature of the model, the cause of this discrepancy will be tricky to pin down.

One of the first things tested was the implementation of the surface anchoring. Past modelling of this cell involved the use of Dirichlet boundary conditions, rather than a surface free-energy term. This possibility was explored in two ways. First, the model was run using Dirichlet boundary conditions instead of the surface free-energy term. This resulted in the model being unable to converge for even a single time step. Second, in the limit of $\alpha \to \inf$the surface free-energy term acts essentially as a Dirichlet boundary conditions; even the smallest deviation from the preferred direction would incur an infinite free-energy contribution. Thus, the anchoring strength was varied in increments of one order of magnitude, starting from its value of 10^{-4} J/m all the way up to 10^{-1} J/m. At values of 10^{-4} J/m and 10^{-3} J/m the results were essentially the same. Increasing the strength further to 10^{-2} J/m resulted in previously unobserved defects forming on the surface of the domain. These defects could not be relaxed out by forcing the model to continue performing timesteps beyond the usual equilibrium criteria. Finally, increasing the strength to 10^{-1} J/m resulted in the model being unable to converge for even one time step. These stronger anchoring strengths were tested both from the original initial condition, molecules all vertical, and by using the equilibrium condition of a lower anchoring strength model as the initial condition for a stronger anchoring strength one. I.e. the equilibrium condition from the 10^{-4} J/m run was used as the initial condition for the 10^{-3} J/m run. This had no effect on the final result.

Next, the material properties of the nematic were tested. As mentioned earlier, previous modelling work used E7 and an unspecified nematic. Both appeared to obtain qualitatively similar textures despite using different nematic materials. Nevertheless, the possibility that using 5CB was the cause of the issue was investigated. Unfortunately, a significant number of material parameters were not available for either of the two materials. For E7 this means

that values not found in literature, and for the unspecified nematic is was impossible to even search. The missing parameters for both material are: T, a_0, b, c, μ_r, and k_{24}. Additionally, the value of T_{NI} was unknown for the unspecified material. In order to perform the modelling, something had to be used for these missing parameters, the values used in each case were those from 5CB. The LC parameters used for modelling with E7 and the unspecified material are in Table A.2 and Table A.3, respectively. Naturally, combining parameters from two different materials reduces the physicality of any modelling results, and does not rule out the possibility that the parameters are the cause. Nevertheless this would still provide valuable information as to whether different material parameters would substantially impact the texture. In short, they did not.

The next thing tested were different initial conditions. Given the highly non-linear nature of the model, the initial conditions can still play an important role, even given the transient evolution formulation of the model. As such, two changes were tried to the initial condition. First, the electric potential initial condition was set to 0 everywhere and the electric potential of the electrodes was slowly ramped up. Second, rather than starting with a vertical orientation as the initial condition, the isotropic state was used; i.e. $Q_{ij} = 0$ everywhere. Neither of these changes brought the final results closer to the publish ones.

Following this were different electric potential differences between the electrodes. The original paper uses 14V, and given that the modelling in this thesis used a different LC, perhaps a different electric potential difference also had to be used. The different electric potential tested are: 6, 10, 28, 40, and 100V. These different voltage had an impact of the resulting texture, but not in a beneficial way. The resulting textures were simply more weakly or strongly oriented versions of the same texture as provided earlier.

6.5 Summary

Having successfully modelled the texture and cross-polarization microscopy results of the TN and IPS cell, it was time to model a LCAL. The criteria used to choose a LCAL design out of the many designs identified in the literature review were: the availability of published results, the modelling requirements of the design, and the ease of production. Based on these criteria, the LCAL design known as the HMD cell was chosen. It uses IPS electrodes on both surfaces, and functions as a pair of stacked cylindrical lenses.

Published modelling results for this cell exist in literature, they were discussed and used for comparison. Unfortunately, the approach taken in modelling the cell in the literature work is too heavily dependant on prior knowledge of experimental results. Additionally,

the model employs too many simplifying assumptions to be of use for predicting the texture of other LCALs. Nevertheless, the results from this model were in agreement with experimental results, and were thus of use for comparing against the equilibrium texture of this model.

Thus, the HMD cell was modelled with the electrodes turned on, and the resulting texture was compared to that from literature. Upon comparison, it was observed that the textures were similar in some ways, but differed substantially from each other. Both the results from this work and from literature had diagonal regions through the cell where the molecules remained perpendicular to the surface. This region was due to the interaction between the anchoring conditions of the cell and the electric field. By preferring starting in a homeotropic orientation, the LC along the cell diagonals were mostly perpendicular to the electric field lines, and thus experience little torque. However, after this similarity, the rest of the texture was different.

Given the difference in texture, it was expected that the cross-polarization microscopy results would also be different. This expectation bore out, the cross-polarization microscopy results from this work were substantially different from the published results, both experimental and modelling ones.

In an attempt to identify the source of this discrepancy, multiple parts of the model and modelling parameters were investigated. The implementation of the surface anchoring was changed, both by using Dirichlet boundary conditions and by increasing the anchoring strength of the surface free-energy term. Next, the material parameters of the nematic were changed; two different nematics based on published papers working with the HMD cell were used. The changes to the material parameters did not address the issue. Next, the initial condition was tested. The initial condition for the electric potential was changed to start at 0V everywhere in the domain. The initial condition for orientation was also tested, starting it in the isotropic phase. Neither of these changes made a difference. Finally, the applied electric potential difference was varied over a range of 6–100V; none of the tested values improved the texture.

The source of discrepancy has not yet been identified.

Chapter 7

Conclusions

7.1 Conclusions

In this work, a general model for thermotropic nematic liquid crystals based on the Landau-de Gennes theory was implemented and used to study the texture of liquid crystal adaptive lenses. A general version of this model was used, without the common simplifications such as hard anchoring, fewer elastic constant approximations, or the use of geometric symmetry. This nematic model was coupled with a model for the electric field within the cell, and the two were solved simultaneously. In order to solve the nematic model, it was converted from a free-energy functional into an Euler-Lagrange PDE, and then into a transient PDE. Solving these PDEs was done using the method of lines for temporal discretization, and the finite element method for spatial discretization.

The validity of the implemented model was first verified by modelling two important LCD cells, the TN and IPS cell. The TN cell was modelled both with the electrodes off and with them on. In both cases the correct equilibrium texture was obtained. Modelling light propagation with cross-polarization microscopy produced the correct results, a bright cell when the electrodes were off and a dark one when they were on. Next, the IPS cell was also modelled with the electrodes turned off and turned on. Again, the correct equilibrium result was obtained, and the same twisted texture was obtained when the electrodes were turned off, and the twist was unwound when the electrodes were turned on. Performing the polarized microscopy modelling yielded the correct dark state when the electrodes were turned off as well as the correct non-uniformly bright state when the electrodes were turned on.

Having successful reproduced the expected texture and cross-polarization microscopy results, the model was applied to a LCAL. The HMD cell was chosen based on three criteria: 1) the availability of published results, 2) the modelling requirements, and 3) the ease of manufacture. It was modelled with the electrodes turned on, however the resulting texture did not agree with previously published modelling results. When the cross-polarization microscopy was performed on the HMD cell, the results of this work did not agree with the published experimental nor published modelling results.

An investigation into the cause of these was performed, but the cause of the discrepancy has not been identified.

7.2 Recommendations

Firstly, since the presented model produced texture and cross-polarization results for the HMD cell which were not in agreement with publish experimental and modelling results, work should continue in identifying the cause of this discrepancy and addressing it.

Having addressed that discrepancy, the next recommendations involve expanding the functionality to the model based on the results of the literature review:

- First, use a more general model for the electromagnetic field, specifically: account for multiple frequencies in the electric field, account for the frequency dependence of ε_{ij}, and account for dissipation. This would allow for the modelling of frequency controlled lenses.
- Next, implement adaptive mesh refinement. This would allow for the accurate modelling of any defects that could form in other designs, without wasting computational resources my having a fine mesh in areas where it is not needed.
- Finally, augment the model to handle multiple domains. Without this ability, the modelling of LCALs would be limited to simple designs and of little use to research or industry.

Two further recommendations are given The first is to augment the finite element back-end in order to run on GPUs. This change would speed up modelling by almost an order of magnitude without introducing simplifications [56]. And, finally, to improve the optical modelling by incorporating predictions of the LCALs optical properties (such as focal length and aberrations).

References

[1] Darko Vasiljević. *Classical and Evolutionary Algorithms in the Optimization of Optical Systems*. Springer US : Imprint : Springer, Boston, MA, 2002.

[2] Tamron USA, Inc. 28-75mm F/2.8 Di III RXD. https://www.tamron-usa.com/product/lenses/a036.html.

[3] Leica Camera AG. SUPER-VARIO-ELMAR-SL 16-35 f/3.5-4.5 ASPH. https://us.leica-camera.com/Photography/Leica-SL/SL-Lenses/Vario-Lenses/Super-Vario-Elmar-SL-16-35.

[4] Hongwen Ren and Shin-Tson Wu. *Introduction to Adaptive Lenses*. Wiley Series in Pure and Applied Optics. Wiley, Hoboken, N.J, 2012. OCLC: ocn759177357.

[5] Carlos Mastrangelo, Fariha Khan, Nazmul Hasan, Chayanjit Ghosh, Tridib Ghosh, Hanseup Kim, and Mohit Karkhanis. Lightweight smart autofocusing eyeglasses. In Wibool Piyawattanametha, Yong-Hwa Park, and Hans Zappe, editors, *MOEMS and Miniaturized Systems XVII*, page 6, San Francisco, United States, February 2018. SPIE.

[6] C. Zhang, M. Gao, N. Diorio, W. Weissflog, U. Baumeister, S. Sprunt, J. T. Gleeson, and A. Jákli. Direct Observation of Smectic Layers in Thermotropic Liquid Crystals. *Physical Review Letters*, 109(10), September 2012.

[7] Fred Fu. *Formation and Field-Switching Dynamics of Nematic Droplets*. PhD thesis, University of Waterloo, Waterloo, Ontario, Canada, 2017.

[8] Jake Ferguson. *Field-Orientation Coupling Effects in Nematic Liquid Crystal Cells*. PhD thesis, University of Waterloo, Waterloo, Ontario, Canada, 2019.

[9] Oleg Alexandrov. Snell's Law. https://commons.wikimedia.org/wiki/File:Snells_law2.svg, December 2007.

[10] Rudolf Kingslake and R. Barry Johnson. *Lens Design Fundamentals*. Academic Press, Ansterdam ; Boston, 2nd ed edition, 2010.

[11] James T. Shipman, Jerry D. Wilson, and Aaron W. Todd. *An Introduction to Physical Science*. Houghton Mifflin, Boston, 12th ed edition, 2009.

[12] Justin Peatross and Michael J Ware. *Physics of Light and Optics*. Brigham Young University, Department of Physics, Provo, Utah, 2015 edition edition, 2016.

[13] Pochi Yeh and Claire Gu. *Optics of Liquid Crystal Displays*. Wiley Series on Pure and Applied Optics. Wiley, Hoboken, N.J, 2nd ed., updated ed edition, 2010. OCLC: ocn317457287.

[14] Ernst Lueder. *Liquid Crystal Displays: Addressing Schemes and Electro-Optical Effects*. Wiley-SID Series in Display Technology. Wiley, Chichester, West Sussex, U.K, 2nd ed edition, 2010. OCLC: ocn465366080.

[15] Gareth P. Alexander, Bryan Gin-ge Chen, Elisabetta A. Matsumoto, and Randall D. Kamien. Colloquium: Disclination loops, point defects, and all that in nematic liquid crystals. *Reviews of Modern Physics*, 84(2):497–514, 2012.

[16] Patrick Oswald and Pawel Pieranski. *Nematic and Cholesteric Liquid Crystals Concepts and Physical Properties Illustrated by Experiments*. Taylor & Francis, Boca Raton, 2005. OCLC: 939247049.

[17] Iztok Bajc, Frédéric Hecht, and Slobodan Žumer. A mesh adaptivity scheme on the Landau–de Gennes functional minimization case in 3D, and its driving efficiency. *Journal of Computational Physics*, 321:981–996, September 2016.

[18] Nasser Mohieddin Abukhdeir and Alejandro D. Rey. Edge dislocation core structure in lamellar smectic-A liquid crystals. *Soft Matter*, 6(6):1117, 2010.

[19] N. Aoki, S. Komura, T. Furuhashi, M. Adachi, O. Itou, T. Miyazawa, and M. Ohkura. Advanced IPS technology for mobile applications. *Journal of the Society for Information Display*, 15(1):23, 2007.

[20] DrBob. Diverging Lens. https://commons.wikimedia.org/wiki/File:Lens1b.svg, March 2006.

[21] DrBob. Converging Lens. https://commons.wikimedia.org/wiki/File:Lens1.svg, March 2006.

[22] Tigran V. Galstian. *Smart Mini-Cameras*. Smart Mini-Cameras. CRC Press, September 2013.

[23] Pko. Fresnel Lens. https://en.wikipedia.org/wiki/File:Fresnel_lens.svg, April 2006.

[24] Barbara K. Pierscionek and Justyn W. Regini. The gradient index lens of the eye: An opto-biological synchrony. *Progress in Retinal and Eye Research*, 31(4):332–349, July 2012.

[25] Tigran Galstian, Karen Asatryan, Vladimir Presniakov, Aram Bagramyan, Armen Zohrabyan, and Simon CAREAU. Flat liquid crystal layered fresnel lens device, November 2017.

[26] Marenori Kawamura, Eiji Yumoto, and Shunsuke Ishikuro. 3-D Microscope System by Using a Liquid Crystal Lens. *International Journal of Optomechatronics*, 7(3):149–159, July 2013.

[27] Tamasflex. Cooke Triplet. https://commons.wikimedia.org/wiki/File:Cooke.png, October 2010.

[28] Joseph M. Geary. *Introduction to Lens Design: With Practical ZEMAX Examples*. Willmann-Bell, Richmond, Va, 2002.

[29] Lambda Research Corporation. OSLO Optimization. https://www.lambdares.com/support/oslo-optimization/, 2019.

[30] Donald Dilworth and Institute of Physics (Great Britain). *Lens Design: Automatic and Quasi-Autonomous Computational Methods and Techniques*. IOP Publishing, 2018.

[31] Richard William Llewellyn James. *Modelling of High Resolution Liquid Crystal Devices*. Ph.D., University of London, University College London (United Kingdom), England, 2006.

[32] Apala Majumdar. Equilibrium order parameters of nematic liquid crystals in the Landau-de Gennes theory. *European Journal of Applied Mathematics*, 21(2):181–203, April 2010.

[33] F. C. Frank. I. Liquid crystals. On the theory of liquid crystals. *Discussions of the Faraday Society*, 25:19, 1958.

[34] P.G. de Gennes and J Prost. *The Physics of Liquid Crystals*. Oxford University Press, New York, second edition, 1995.

[35] RD Polak, GP Crawford, BC Kostival, JW Doane, and S Žumer. Optical determination of the saddle-splay elastic constant k 24 in nematic liquid crystals. *Physical Review E*, 49(2):R978, 1994.

[36] Hiroyuki Mori, Eugene C. Gartland, Jack R. Kelly, and Philip J. Bos. Multidimensional director modeling using the Q tensor representation in a liquid crystal cell and its application to the it cell with patterned electrodes. *Japanese Journal of Applied Physics*, 38(1):135–146, 1999.

[37] A. Rapini and M. Papoular. Distorsion d'une lamelle nématique sous champ magnétique conditions d'ancrage aux parois. *Le Journal de Physique Colloques*, 30(C4):C4–54–C4–56, nov 1969.

[38] E. Willman, F.A. Fernandez, R. James, and S.E. Day. Modeling of Weak Anisotropic Anchoring of Nematic Liquid Crystals in the Landau–de Gennes Theory. *IEEE Transactions on Electron Devices*, 54(10):2630–2637, October 2007.

[39] Dwight W. Berreman. Variable focus liquid crystal lens system, February 1980.

[40] Susumu Sato. Liquid-Crystal Lens-Cells with Variable Focal Length. *Japanese Journal of Applied Physics*, 18(9):1679–1684, September 1979.

[41] S. T. Cleverly Kowel and Dennis S. Cleverly. A liquid crystal adaptive lens. In *Optical Information Processing for Aerospace Applications*, pages 329–339, Hampton, Virginia, December 1981. NASA.

[42] Stephen T. Kowel, Philipp Kornreich, and Akbar Nouhi. Adaptive spherical lens. *Applied Optics*, 23(16):2774, August 1984.

[43] Stephen T. Kowel, Dennis S. Cleverly, and Philipp G. Kornreich. Focusing by electrical modulation of refraction in a liquid crystal cell. *Applied Optics*, 23(2):278, January 1984.

[44] C. W. Fowler and E. S. Pateras. Liquid crystal lens review. *Ophthalmic and Physiological Optics*, 10(2):186–194, 1990.

[45] G. E. Nevskaya and M. G. Tomilin. Adaptive lenses based on liquid crystals. *Journal of Optical Technology*, 75(9):563–573, September 2008.

[46] Hung-Chun Lin, Ming-Syuan Chen, and Yi-Hsin Lin. A Review of Electrically Tunable Focusing Liquid Crystal Lenses. *Transactions on Electrical and Electronic Materials*, 12(6):234–240, December 2011.

[47] Yi-Hsin Lin, Yu-Jen Wang, and Victor Reshetnyak. Liquid crystal lenses with tunable focal length. *Liquid Crystals Reviews*, 5(2):111–143, July 2017.

[48] Se-Um Kim, Jun-Hee Na, Chiwoo Kim, and Sin-Doo Lee. Design and fabrication of liquid crystal-based lenses. *Liquid Crystals*, 44(12-13):2121–2132, 2017.

[49] José Francisco Algorri, Dimitrios C. Zografopoulos, Virginia Urruchi, and José Manuel Sánchez-Pena. Recent Advances in Adaptive Liquid Crystal Lenses. *Crystals*, 9(5):272, May 2019.

[50] Chao-Te Lee, Yan Li, Hoang-Yan Lin, and Shin-Tson Wu. Design of polarization-insensitive multi-electrode GRIN lens with a blue-phase liquid crystal. *Optics Express*, 19(18):17402, August 2011.

[51] Fan Chu, Hu Dou, Gui-Peng Li, Ya-Li Song, Lei Li, and Qiong-Hua Wang. A polarisation-independent blue-phase liquid crystal lens array using gradient electrodes. *Liquid Crystals*, 45(5):715–720, April 2018.

[52] Yun Ho Kim, Dong Ki Yoon, Hyeon Su Jeong, Oleg D. Lavrentovich, and Hee-Tae Jung. Smectic Liquid Crystal Defects for Self-Assembling of Building Blocks and Their Lithographic Applications. *Advanced Functional Materials*, 21(4):610–627, February 2011.

[53] Francesca Serra, Mohamed A. Gharbi, Yimin Luo, Iris B. Liu, Nathan D. Bade, Randall D. Kamien, Shu Yang, and Kathleen J. Stebe. Curvature-Driven, One-Step Assembly of Reconfigurable Smectic Liquid Crystal "Compound Eye" Lenses. *Advanced Optical Materials*, 3(9):1287–1292, September 2015.

[54] Hui Li, Fan Pan, Yuntao Wu, Yanduo Zhang, and Xiaolin Xie. Electrically Tunable Binary-Phase Fresnel Lens Based on Polymer Dispersed Liquid Crystal. *Materials Science*, 23(2), May 2017.

[55] Yuki Harada, Daisuke Koyama, Marina Fukui, Akira Emoto, Kentaro Nakamura, and Mami Matsukawa. Molecular Orientation in a Variable-Focus Liquid Crystal Lens Induced by Ultrasound Vibration. *Scientific Reports*, 10(1):6168, April 2020.

[56] Miha Čančula. *Mutually Coupled Flow of Light and Liquid Crystal Ordering*. PhD thesis, University of Ljubljana, Ljubljana, 2017.

[57] Erwen Mei and Daniel A. Higgins. Electric-field-induced ion migration in polymer-dispersed liquid- crystal films observed by near-field scanning optical microscopy. *Applied Physics Letters*, 75(3):430–432, July 1999.

[58] Bin Wang, Ye Mao, and S. Sato. Liquid crystal lens with focal length variable from negative to positive values. *IEEE Photonics Technology Letters*, 18(1):79–81, January 2006.

[59] Tom Vanackere, Tom Vandekerckhove, Elke Claeys, John Puthenparampil George, Kristiaan Neyts, and Jeroen Beeckman. Improvement of liquid crystal tunable lenses with weakly conductive layers using multifrequency driving. *Optics Letters*, 45(4):1001–1004, February 2020.

[60] Philip J. W. Hands, Andrew K. Kirby, and Gordon D. Love. Adaptive modally addressed liquid crystal lenses. In *Liquid Crystals VIII*, volume 5518, pages 136–143. International Society for Optics and Photonics, October 2004.

[61] Oleg Pishnyak, Susumu Sato, and Oleg D. Lavrentovich. Electrically tunable lens based on a dual-frequency nematic liquid crystal. *Applied Optics*, 45(19):4576, July 2006.

[62] Yung-Yuan Kao, Paul C.-P. Chao, and Chieh-Wen Hsueh. A new low-voltage-driven GRIN liquid crystal lens with multiple ring electrodes in unequal widths. *Optics Express*, 18(18):18506, August 2010.

[63] Afsoon Jamali, Douglas Bryant, Yanli Zhang, Anders Grunnet-Jepsen, Achintya Bhowmik, and Philip J. Bos. Design of a large aperture tunable refractive Fresnel liquid crystal lens. *Applied Optics*, 57(7):B10, March 2018.

[64] Zhan He, Toshiaki Nose, and Susumu Sato. Cylindrical Liquid Crystal Lens and Its Applications in Optical Pattern Correlation Systems. *Japanese Journal of Applied Physics*, 34(Part 1, No. 5A):2392–2395, May 1995.

[65] Yi-Hsin Lin, Hongwen Ren, Kuan-Hsu Fan-Chiang, Wing-Kit Choi, Sebastian Gauza, Xinyu Zhu, and Shin-Tson Wu. Tunable-Focus Cylindrical Liquid Crystal Lenses. *Japanese Journal of Applied Physics*, 44(1R):243, January 2005.

[66] J. F. Algorri, V. Urruchi, N. Bennis, J. M. Sánchez-Pena, and J. M. Otón. Tunable liquid crystal cylindrical micro-optical array for aberration compensation. *Optics Express*, 23(11):13899–13915, June 2015.

[67] Rifat Ata Mustafa Hikmet, Ties Van Bommel, Thomas Caspar Kraan, Leon Hendrikus Christiaan Kusters, Siebe Tjek De Zwart, Oscar Hendrikus Willemsen, and Marcellinus Petrus Carolus Michael Krijn. Beam-shaping device, June 2010.

[68] S P Kotova, A M Mayorova, and S A Samagin. Tunable 4-channel LC focusing device: Summarized results and additional functional capabilities. *Journal of Optics*, 17(5):055602, May 2015.

[69] Toshiaki Nose and Susumu Sato. A liquid crystal microlens obtained with a non-uniform electric field. *Liquid Crystals*, 5(5):1425–1433, January 1989.

[70] Oleksandr Sova and Tigran Galstian. Liquid crystal lens with optimized wavefront across the entire clear aperture. *Optics Communications*, 433:290–296, February 2019.

[71] Karen Asatryan, Vladimir Presnyakov, Amir Tork, Armen Zohrabyan, Aram Bagramyan, and Tigran Galstian. Optical lens with electrically variable focus using an optically hidden dielectric structure. *Optics Express*, 18(13):13981, June 2010.

[72] Oleksandr Sova, Victor Reshetnyak, and Tigran Galstian. Theoretical analyses of a liquid crystal adaptive lens with optically hidden dielectric double layer. *Journal of the Optical Society of America A*, 34(3):424, March 2017.

[73] Wei-Min Huang, Ren-Kai Yang, and Guo-Dung J Su. Variable focus microlens array with curved electrodes. *Journal of Micromechanics and Microengineering*, 27(5):055003, May 2017.

[74] Li-Lan Tian, Fan Chu, Hu Dou, Qiong-Hua Wang, and Lei Li. Short-focus nematic liquid crystal microlens array with a dielectric layer. *Liquid Crystals*, 47(1):76–82, January 2020.

[75] Liwei Li, Doug Bryant, and Philip J. Bos. Liquid crystal lens with concentric electrodes and inter-electrode resistors. *Liquid Crystals Reviews*, 2(2):130–154, July 2014.

[76] C. Lin, H. Huang, and J. Wang. Polarization-Independent Liquid-Crystal Fresnel Lenses Based on Surface-Mode Switching of 90 Twisted-Nematic Liquid Crystals. *IEEE Photonics Technology Letters*, 22(3):137–139, February 2010.

[77] Yimin Lou, Linsen Chen, Chinhua Wang, and Su Shen. Tunable-focus liquid crystal Fresnel zone lens based on harmonic diffraction. *Applied Physics Letters*, 101(22):221121, November 2012.

[78] Wen-Chi Hung, Yu-Jen Chen, Chia-Huey Lin, I-Min Jiang, and Tzu-Fang Hsu. Sensitive voltage-dependent diffraction of a liquid crystal Fresnel lens. *Applied Optics*, 48(11):2094, April 2009.

[79] Yoonseuk Choi, Yeun-Tae Kim, Sin-Doo Lee, and Jae-Hoon Kim. Polarization Independent Static Microlens Array in the Homeotropic Liquid Crystal Configuration. *Molecular Crystals and Liquid Crystals*, 433(1):191–197, June 2005.

[80] Susumu Sato, Akira Sugiyama, and Rumiko Sato. Variable-Focus Liquid-Crystal Fresnel Lens. *Japanese Journal of Applied Physics*, 24(8A):L626, August 1985.

[81] Mao Ye and Susumu Sato. Liquid Crystal Lens with Insulator Layers for Focusing Light Waves of Arbitrary Polarizations. *Japanese Journal of Applied Physics*, 42(Part 1, No. 10):6439–6440, October 2003.

[82] Ye Mao, Bin Wang, and S. Sato. Polarization-independent liquid crystal lens with four liquid crystal layers. *IEEE Photonics Technology Letters*, 18(3):505–507, February 2006.

[83] Yung-Hsiang Hsu, Tzu-Hsiang Kao, Chun-Yu Chien, and Chia-Rong Sheu. Polarisation-independent liquid crystal lens array with additional dielectric films over self-aligned dual hole-patterned electrodes. *Liquid Crystals*, 0(0):1–9, January 2020. _eprint: https://doi.org/10.1080/02678292.2019.1710867.

[84] Che-Ju Hsu, Chen-Hau Liao, Bao-Long Chen, Shang-Yi Chih, and Chi-Yen Huang. Polarization-insensitive liquid crystal microlens array with dual focal modes. *Optics Express*, 22(21):25925–25930, October 2014.

[85] Gordon D. Love. Liquid-crystal phase modulator for unpolarized light. *Applied Optics*, 32(13):2222, May 1993.

[86] Tigran Galstian and Karen Allahverdyan. Focusing unpolarized light with a single-nematic liquid crystal layer. *Optical Engineering*, 54(2):025104, February 2015.

[87] Chi-Wei Chiu, Yu-Cheng Lin, Paul C.-P. Chao, and Andy Y.-G. Fuh. Achieving high focusing power for a large aperture liquid crystal lens with novel hole-and-ring electrodes. *Optics Express*, 16(23):19277, November 2008.

[88] Mao Ye, Bin Wang, and Susumu Sato. Double-Layer Liquid Crystal Lens. *Japanese Journal of Applied Physics*, 43(No. 3A):L352–L354, February 2004.

[89] Bin Wang, Mao Ye, and Susumu Sato. Liquid crystal lens with stacked structure of liquid-crystal layers. *Optics Communications*, 250(4):266–273, June 2005.

[90] Shug-June Hwang, Yi-Ming Shieh, and Kuo-Ren Lin. Liquid Crystal Microlens Using Nanoparticle-Induced Vertical Alignment. *Journal of Nanomaterials*, 2015:1–7, 2015.

[91] Hu Dou, Fan Chu, Yu-Qiang Guo, Li-Lan Tian, Qiong-Hua Wang, and Yu-Bao Sun. Large aperture liquid crystal lens array using a composited alignment layer. *Optics Express*, 26(7):9254, April 2018.

[92] Rui Li, Fan Chu, Hu Dou, Li-Lan Tian, Wen-Yi Hou, Lei Li, and Qiong-Hua Wang. Double-layer liquid crystal lens array with composited dielectric layer. *Liquid Crystals*, 0(0):1–7, July 2019.

[93] Rui Li, Fan Chu, Li-Lan Tian, Xiao-Qing Gu, Xiang-Yu Zhou, and Qiong-Hua Wang. Short focal length tunable liquid crystal lenticular lens array based on fringe field effect. *Journal of the Society for Information Display*, March 2020.

[94] Rui Li, Fan Chu, Hu Dou, Li-Lan Tian, Wen-Yi Hou, Lei Li, and Qiong-Hua Wang. Double-layer liquid crystal lens array with composited dielectric layer. *Liquid Crystals*, 47(2):248–254, January 2020.

[95] Wen Huang, Peng Li, Siming Li, and Qing Li. Research on Large Aperture Liquid Crystal Lens. *SID Symposium Digest of Technical Papers*, 51(S1):147–150, 2020.

[96] G. Panasyuk and D. W. Allender. Model for the director and electric field in liquid crystal cells having twist walls or disclination lines. *Journal of Applied Physics*, 91(12):9603, 2002.

[97] Marenori Kawamura, Mao Ye, and Susumu Sato. Transient Properties of a Liquid Crystal Optical Device with an Elliptical Intensity Distribution. *Japanese Journal of Applied Physics*, 47(8):6404–6406, August 2008.

[98] Xiangjie Zhao, Cangli Liu, Dayong Zhang, and Yongquan Luo. Modeling and design of an optimized patterned electrode liquid crystal microlens array with dielectric slab. *Optik*, 124(23):6132–6139, December 2013.

[99] J. F. Algorri, G. D. Love, and V. Urruchi. Modal liquid crystal array of optical elements. *Optics Express*, 21(21):24809–24818, October 2013.

[100] Amir Hassanfiroozi, Yi-Pai Huang, Bahram Javidi, and Han-Ping D. Shieh. Hexagonal liquid crystal lens array for 3D endoscopy. *Optics Express*, 23(2):971, January 2015.

[101] T. Galstian, O. Sova, K. Asatryan, V. Presniakov, A. Zohrabyan, and M. Evensen. Optical camera with liquid crystal autofocus lens. *Optics Express*, 25(24):29945, November 2017.

[102] Oleksandr Sova and Tigran Galstian. Modal control refractive Fresnel lens with uniform liquid crystal layer. *Optics Communications*, 474:126056, November 2020.

[103] Mengyang Yang, S. E. Day, and F. A. Fernández. Modelling the optics of high resolution liquid crystal devices by the finite differences in the frequency domain method. In *2017 International Workshop on Electromagnetics: Applications and Student Innovation Competition*, pages 141–143, May 2017.

[104] Michinori Honma, Toshiaki Nose, and Susumu Sato. Enhancement of Numerical Aperture of Liquid Crystal Microlenses Using a Stacked Electrode Structure. *Japanese Journal of Applied Physics*, 39(Part 1, No. 8):4799–4802, August 2000.

[105] Guoqiang Li, David L. Mathine, Pouria Valley, Pekka Äyräs, Joshua N. Haddock, M. S. Giridhar, Gregory Williby, Jim Schwiegerling, Gerald R. Meredith, Bernard Kippelen, Seppo Honkanen, and Nasser Peyghambarian. Switchable electro-optic diffractive lens with high efficiency for ophthalmic applications. *Proceedings of the National Academy of Sciences*, 103(16):6100–6104, April 2006.

[106] eVision. eVision Optics. www.evisionoptics.com.

[107] DeepOptics. DeepOptics. http://www.deepoptics.com/do_site/.

[108] Harry E. Milton, Helen F. Gleeson, Philip B. Morgan, John W. Goodby, Stephen Cowling, and John H. Clamp. Switchable liquid crystal contact lenses: Dynamic vision for the ageing eye. In *Emerging Liquid Crystal Technologies IX*, volume 9004, page 90040H. International Society for Optics and Photonics, February 2014.

[109] James Bailey, Philip Morgan, Helen Gleeson, and J. Jones. Switchable Liquid Crystal Contact Lenses for the Correction of Presbyopia. *Crystals*, 8(1):29, January 2018.

[110] Gleb Vdovin, Mikhail Loktev, and Alexander Naumov. On the possibility of intraocular adaptive optics. *Optics Express*, 11(7):810, April 2003.

[111] Aleksey N. Simonov, Gleb Vdovin, and Mikhail Loktev. Liquid-crystal intraocular adaptive lens with wireless control. *Optics Express*, 15(12):7468, 2007.

[112] Tigran Galstian and Howard Earhart. Reprogrammable tuneable liquid crystal lens intraocular implant and methods therefor, April 2016.

[113] Arutyun Bagramyan, Tigran Galstian, and Armen Saghatelyan. Motion-free endoscopic system for brain imaging at variable focal depth using liquid crystal lenses. *Journal of Biophotonics*, 10(6-7):762–774, March 2016.

[114] Yi-Pai Huang, Po-Yuan Hsieh, Amir Hassanfiroozi, Chao-Yu Chu, Yun Hsuan, Manuel Martinez, and Bahram Javidi. Liquid crystal lens array for 3D microscopy and endoscope application. In *Three-Dimensional Imaging, Visualization, and Display 2016*, volume 9867, page 98670W. International Society for Optics and Photonics, June 2016.

[115] Apple Inc. iPhone. https://www.apple.com/ca/iphone/.

[116] Pouria Valley, David L. Mathine, Mohammad Reza Dodge, Jim Schwiegerling, Gholam Peyman, and N. Peyghambarian. Tunable-focus flat liquid-crystal diffractive lens. *Optics Letters*, 35(3):336, February 2010.

[117] Mao Ye, Bin Wang, Masaru Uchida, Satoshi Yanase, Shingo Takahashi, and Susumu Sato. Focus tuning by liquid crystal lens in imaging system. *Applied Optics*, 51(31):7630, November 2012.

[118] Mareddi Bharath Kumar, Daekyung Kang, Jihoon Jung, Hongsik Park, Joonku Hahn, Muhan Choi, Jin-Hyuk Bae, Hyunmin Kim, and Jonghoo Park. Compact vari-focal augmented reality display based on ultrathin, polarization-insensitive, and adaptive liquid crystal lens. *Optics and Lasers in Engineering*, 128:106006, May 2020.

[119] Margaret Harris. A better virtual experience. *Physics World*, May 2018.

[120] Yu-Jen Wang and Yi-Hsin Lin. An optical system for augmented reality with electrically tunable optical zoom function and image registration exploiting liquid crystal lenses. *Optics Express*, 27(15):21163–21172, July 2019.

[121] Mao Ye, Bin Wang, and Susumu Sato. Liquid crystal lens with focus movable in focal plane. *Optics Communications*, 259(2):710–722, March 2006.

[122] Simon Thibault, Alexandre Baril, and Tigran Glastian. Smart lighting using a liquid crystal modulator. In R. Barry Johnson, Virendra N. Mahajan, and Simon Thibault, editors, *Current Developments in Lens Design and Optical Engineering XVIII*, page 21, San Diego, United States, August 2017. SPIE.

[123] LensVector. LensVector. https://www.lensvector.com.

[124] W. Y. Li and S. H. Chen. Simulation of normal anchoring nematic droplets under electrical fields. *JAPANESE JOURNAL OF APPLIED PHYSICS PART 1-REGULAR PAPERS SHORT NOTES & REVIEW PAPERS*, 38(3A):1482–1487, March 1999.

[125] Anders Logg, Kent-Andre Mardal, and Garth Wells, editors. *Automated Solution of Differential Equations by the Finite Element Method: The FEniCS Book*. Number 84 in Lecture Notes in Computational Science and Engineering. Springer, Heidelberg, 2012.

[126] Andrej Petelin. IJSComplexMatter/dtmm: Version 0.4.0. Zenodo, May 2020.

[127] Dwight Berreman. Optics in Stratified and Anisotropic Media: 4X4-Matrix Formulation. *Journal of the Optical Society of America*, 62(4):502–510, April 1972.

[128] Robert H. Chen. *Liquid Crystal Displays: Fundamental Physics and Technology*. Wiley-SID Series in Display Technology. Wiley, Hoboken, NJ, 2011. OCLC: 747528205.

[129] Mosaic Documentation Web. Cell Constant of Interdigitated Electrodes. http://www.mosaic-industries.com/embedded-systems/_media/instrumentation/conductivity-meter/generic-sensor-geometry.png, September 2012.

[130] BBCLCD. IPS Pixel. https://commons.wikimedia.org/wiki/File:Diagram_LCD_IPS.jpg, September 2012.

[131] S. H. Lee, H. Y. Kim, S. C. Kim, Y. H. Lee, I. C. Park, B. G. Rho, J. S. Park, C. H. Lee, H. G. Galabova, and D. W. Allender. Multi-Domainlike, Homeotropic Nematic Liquid Crystal Display. *SID Symposium Digest of Technical Papers*, 29(1):702–705, 1998.

[132] Hyang Yul Kim and Seung Hee Lee. Homeotropic multi-domain, November 2000.

[133] Tae-Hoon Choi, Jae-Won Huh, Jae-Hyeon Woo, Jin-Hun Kim, Young-Seo Jo, and Tae-Hoon Yoon. Switching between transparent and translucent states of a two-dimensional liquid crystal phase grating device with crossed interdigitated electrodes. *Optics Express*, 25(10):11275–11282, May 2017.

[134] Giannis D. Ziogos and Emmanouil E. Kriezis. Modeling light propagation in liquid crystal devices with a 3-D full-vector finite-element beam propagation method. *Optical and Quantum Electronics*, 40(10):733–748, December 2008.

[135] G. Panasyuk and D. W. Allender. Approximate description of the three dimensional director and electric field in a liquid crystal display at a high voltage. *Journal of Applied Physics*, 87(2):649–657, January 2000.

[136] G. Panasyuk, D. W. Allender, and J. Kelly. Approximate description of the two-dimensional director field in a liquid crystal display. *Journal of Applied Physics*, 89(9):4777–4786, April 2001.

[137] S. H. Lee, H. Y. Kim, Y. H. Lee, I. C. Park, B. G. Rho, H. G. Galabova, and D. W. Allender. Wide viewing angle, homeotropic nematic liquid-crystal display controlled by effective field. *Applied Physics Letters*, 73(4):470–472, July 1998.

[138] H. J. Coles. Laser and Electric Field Induced Birefringence Studies on the Cyanobiphenyl Homologues. *Molecular Crystals and Liquid Crystals*, 49(3):67–74, October 1978.

[139] A. Bogi and S. Faetti. Elastic, dielectric and optical constants of 4'-pentyl-4-cyanobiphenyl. *Liquid Crystals*, 28(5):729–739, 2001.

[140] David A. Dunmur, Atsuo Fukuda, and Geoffrey R. Luckhurst, editors. *Physical Properties of Liquid Crystals: Nematics*. Number 25 in EMIS Datareviews Series. Institution of Electrical Engineers, London, 2001.

[141] K. Skarp, S. T. Lagerwall, and B. Stebler. Measurements of Hydrodynamic Parameters for Nematic 5CB. *Molecular Crystals and Liquid Crystals*, 60(3):215–236, July 1980.

[142] Paul S. Drzaic. *Liquid Crystal Dispersions*, volume 1 of *Liquid Crystals Series*. World Scientific, 1995.

[143] O. D. Lavrentovich and V. M. Pergamenshchik. Stripe Domain Phase of a Thin Nematic Film and the K_{13} Divergence Term. *Physical Review Letters*, 73(7):979–983, 1994.

[144] J. L. Ericksen. Inequalities in Liquid Crystal Theory. *Physics of Fluids*, 9(6):1205, 1966.

[145] A.Ghanadzadeh Gilani and M.S. Beevers. The Electro-optical kerr effect in eutectic nematic mixtures of E7 and E8. *Journal of Molecular Liquids*, 92(3):217–225, July 2001.

[146] H. Allinson and H. F. Gleeson. Dielectric permittivity properties of a fulgide dye guest-host liquid crystal. *Liquid Crystals*, 19(4):421–425, October 1995.

APPENDICES

Appendix 1: Model Parameters

Table A.1: LC parameters for 5CB

Parameter	Value	Units	Source	Parameter	Value	Units	Source
T^*_{NI}	307.5	K	[138]	L_1	4.28×10^{-12}	J m^{-1}	derived
T	303.5	K	-	L_2	4.28×10^{-12}	J m^{-1}	derived
a_0	1.3×10^5	J m^{-3} K^{-1}	[138]	L_3	2.68×10^{-12}	J m^{-1}	derived
b	1.6×10^6	J m^{-3}	[138]	L_{24}	1.99×10^{-12}	J m^{-1}	derived
c	3.9×10^6	J m^{-3}	[138]	$\varepsilon_\parallel$	18.4	-	[139]
k_{11}	4.45×10^{-12}	J m^{-1}	[138]	$\varepsilon_\perp$	7.2	-	[139]
k_{22}	2.90×10^{-12}	J m^{-1}	[138]	$n_\parallel$	1.69	-	[140]
k_{33}	5.75×10^{-12}	J m^{-1}	[138]	$n_\perp$	1.54	-	[140]
k_{24}	7.75×10^{-13}	J m^{-1}	derived[1]	μ_r	0.055	kg m^{-1}s^{-1}	[141]
				α	10^{-4}	J m^{-2}	[142]

[1]This term is difficult to measure reliably [35, 143]. Instead, a value of $k_{24} = \frac{k_{22}}{4}$ is used in order to satisfy the Eriksen inequalities [144].

[2]Same problem as for 5CB issue, it difficult to measure reliably. Instead a value of $k_{24} = \frac{k_{22}}{4}$ in order to satisfy the Eriksen inequalities [144].

[3]Not provided in the paper, and since the LC was not specified there is no way to find it in literature, assuming it has even been measured. Instead a value of $k_{24} = \frac{k_{22}}{4}$ in order to satisfy the Eriksen inequalities [144].

Table A.2: LC parameters for E7

Parameter	Value	Units	Source	Parameter	Value	Units	Source
T^*_{NI}	328	K	[145]	L_1	3.15×10^{-12}	J m^{-1}	derived
T	320	K	-	L_2	2.65×10^{-12}	J m^{-1}	derived
a_0	1.3×10^5	J m^{-3} K^{-1}	[138]	L_3	9.63×10^{-13}	J m^{-1}	derived
b	1.6×10^6	J m^{-3}	[138]	L_{24}	1.43×10^{-12}	J m^{-1}	derived
c	3.9×10^6	J m^{-3}	[138]	$\varepsilon_\parallel$	15.99	-	[146]
k_{11}	8.10×10^{-12}	J m^{-1}	[140]	$\varepsilon_\perp$	5.76	-	[146]
k_{22}	4.73×10^{-12}	J m^{-1}	[140]	$n_\parallel$	1.69	-	[140]
k_{33}	9.55×10^{-12}	J m^{-1}	[140]	$n_\perp$	1.52	-	[140]
k_{24}	1.18×10^{-13}	J m^{-1}	derived[2]	μ_r	0.055	kg m^{-1}s^{-1}	[141]
				α	10^{-4}	J m^{-2}	[142]

Table A.3: LC parameters used for the unspecified nematic

Parameter	Value	Units	Source	Parameter	Value	Units	Source
T^*_{NI}	307.5	K	[138]	L_1	4.03×10^{-12}	J m^{-1}	derived
T	303.5	K	-	L_2	2.42×10^{-12}	J m^{-1}	derived
a_0	1.3×10^5	J m^{-3} K^{-1}	[138]	L_3	5.32×10^{-12}	J m^{-1}	derived
b	1.6×10^6	J m^{-3}	[138]	L_{24}	1.21×10^{-12}	J m^{-1}	derived
c	3.9×10^6	J m^{-3}	[138]	$\varepsilon_\parallel$	19.4	-	[137]
k_{11}	7×10^{-12}	J m^{-1}	[135]	$\varepsilon_\perp$	12	-	[137]
k_{22}	4×10^{-12}	J m^{-1}	[135]	$n_\parallel$	1.588	-	[137]
k_{33}	1.5×10^{-11}	J m^{-1}	[135]	$n_\perp$	1.5	-	[137]
k_{24}	1×10^{-12}	J m^{-1}	derived[3]	μ_r	0.055	kg m^{-1}s^{-1}	[141]
				α	10^{-4}	J m^{-2}	[142]